

# Sub-second volumetric 3D printing by synthesis of holographic light fields

<https://doi.org/10.1038/s41586-026-10114-5>

Received: 5 February 2025

Accepted: 8 January 2026

Published online: 11 February 2026

Open access

 Check for updates

Xukang Wang<sup>1,2,9</sup>, Yuanzhu Ma<sup>1,2,9</sup>, Yihan Niu<sup>2,3,9</sup>, Bo Xiong<sup>1,2</sup>, Anke Zhang<sup>2,4</sup>, Guoxun Zhang<sup>1,2</sup>, Yifan Chen<sup>1,2</sup>, Wei Wei<sup>5</sup>, Lu Fang<sup>2,3,6,7</sup>✉, Jiamin Wu<sup>1,2,6,7,8</sup>✉ & Qionghai Dai<sup>1,2,6,7</sup>✉

Volumetric additive manufacturing has emerged as a promising technique for the flexible production of complex structures, with diverse applications in engineering, photonics and biology<sup>1,2</sup>. However, present methods still face a trade-off between resolution and volumetric build rate, restricting efficient and flexible production of high-resolution 3D structures. Here we propose a method, called digital incoherent synthesis of holographic light fields (DISH), to generate high-resolution 3D light distributions through continuous multi-angle projections with a high-speed rotating periscope without the requirement of sample rotation. The iterative optimization of the holograms for different angles in DISH maintains 19- $\mu\text{m}$  printing resolution across the 1-cm range that is far beyond the depth of field of the objective and enables high-resolution *in situ* 3D printing of millimetre-scale objects within only 0.6 s. Acrylate materials in a range of viscosities are used to demonstrate the general compatibility of DISH. Integrating DISH with a fluid channel, we achieved mass production of complex and diverse 3D structures within low-viscosity materials, demonstrating its potential for broad applications in diverse fields.

Precise and efficient manufacturing of complex 3D structures is increasingly vital across diverse fields such as structural mechanics<sup>3–5</sup>, photonics<sup>6</sup>, pharmaceuticals<sup>7</sup>, tissue engineering<sup>8,9</sup> and drug screening<sup>10</sup>. Traditional methods such as moulding<sup>11</sup> and phase separation<sup>12</sup> are efficient for mass production but prove costly and time-consuming when modifying structures. 3D printing methods such as stereolithography<sup>13</sup>, digital light processing<sup>14–16</sup> and two-photon polymerization<sup>17–19</sup> offer great flexibility in fabricating intricate 3D designs with high precision, although their efficiency is far from enough for mass production. Efforts have been made to enhance the production rate and reduce the layering effects. Continuous liquid interface production<sup>20,21</sup> uses oxygen inhibition to avoid reciprocating when printing contiguous layers and integrates a continuous roll for batch production<sup>22</sup> but the printing processes are essentially layer-wise. Xolography<sup>23</sup> is a form of volumetric additive manufacturing that moves a light sheet through the stationary resin. Despite its recent update with continuous production using a fluid control system<sup>24</sup>, the dual-colour photoinitiator requires necessary time to revert, which restricts its volumetric build rates.

To address this problem, volumetric 3D printing, exemplified by computed axial lithography (CAL)<sup>1</sup>, emerges as a promising technique to print the entire volume simultaneously using controlled 3D light distributions generated by light patterns from different angles. Because fewer angle numbers used during projection will severely degrade the spatial resolution owing to the missing cone in the frequency domain, akin to computed tomography, present CAL techniques involve the 360° rotation of the sample for high-precision tomographic reconstruction<sup>1,25</sup>.

However, the requirement of sample rotation makes it hard for *in situ* printing and restricts the rotation speed to avoid mechanical vibrations affecting printing resolution and system alignment. In this case, high-viscosity printing ink is usually required to prevent sample sinking during the tens of seconds printing time for millimetre-scale objects, restricting its possibility of integrating flow control to further improve the printing efficiency<sup>1,2,25–28</sup>. Also, when we try to further increase the printing resolution with a high-numerical-aperture (NA) objective for excitation, the diffraction effect of light, once negligible, has now surfaced as a prominent challenge, posing difficulties for maintaining high-precision modulation across a large depth of field<sup>29–31</sup>. Therefore, high-speed, high-throughput successive fabrication of millimetre-scale objects with high resolution remains a systemic challenge.

Here we introduce digital incoherent synthesis of holographic light fields, named DISH, to achieve high-speed, high-resolution volumetric printing of millimetre-scale objects within 1 s. Instead of rotating the sample, we design a rotating periscope with a long-working-distance 0.055-NA objective to deliver high-resolution projections of precisely controlled light fields at a rotation speed of up to 10 rotations s<sup>-1</sup>. Although partially coherent or incoherent light has a shallow depth of field, we use a coherent laser source with a digital micromirror device (DMD) to rapidly generate optimized patterns at up to 17,000 Hz, which can achieve high-resolution modulation even far from the native objective plane without the requirement to mechanically shift the focal plane. Although the DMD cannot directly modulate the phase of the light fields, we develop an iterative algorithm with the wave-optics

<sup>1</sup>Department of Automation, Tsinghua University, Beijing, China. <sup>2</sup>Institute for Brain and Cognitive Sciences, Tsinghua University, Beijing, China. <sup>3</sup>Department of Electronic Engineering, Tsinghua University, Beijing, China. <sup>4</sup>Tsinghua Shenzhen International Graduate School, Tsinghua University, Shenzhen, China. <sup>5</sup>Center for Regeneration and Aging Medicine, The Fourth Affiliated Hospital of School of Medicine and International School of Medicine, International Institutes of Medicine, Zhejiang University, Yiwu, China. <sup>6</sup>School of Artificial Intelligence, Tsinghua University, Beijing, China. <sup>7</sup>Beijing National Research Center for Information Science and Technology, Tsinghua University, Beijing, China. <sup>8</sup>Beijing Visual Science and Translational Eye Research Institute (BERI), Tsinghua Medicine, Tsinghua University, Beijing, China. <sup>9</sup>These authors contributed equally: Xukang Wang, Yuanzhu Ma, Yihan Niu. ✉e-mail: [fanglu@tsinghua.edu.cn](mailto:fanglu@tsinghua.edu.cn); [wujiamin@tsinghua.edu.cn](mailto:wujiamin@tsinghua.edu.cn); [qhdai@tsinghua.edu.cn](mailto:qhdai@tsinghua.edu.cn)

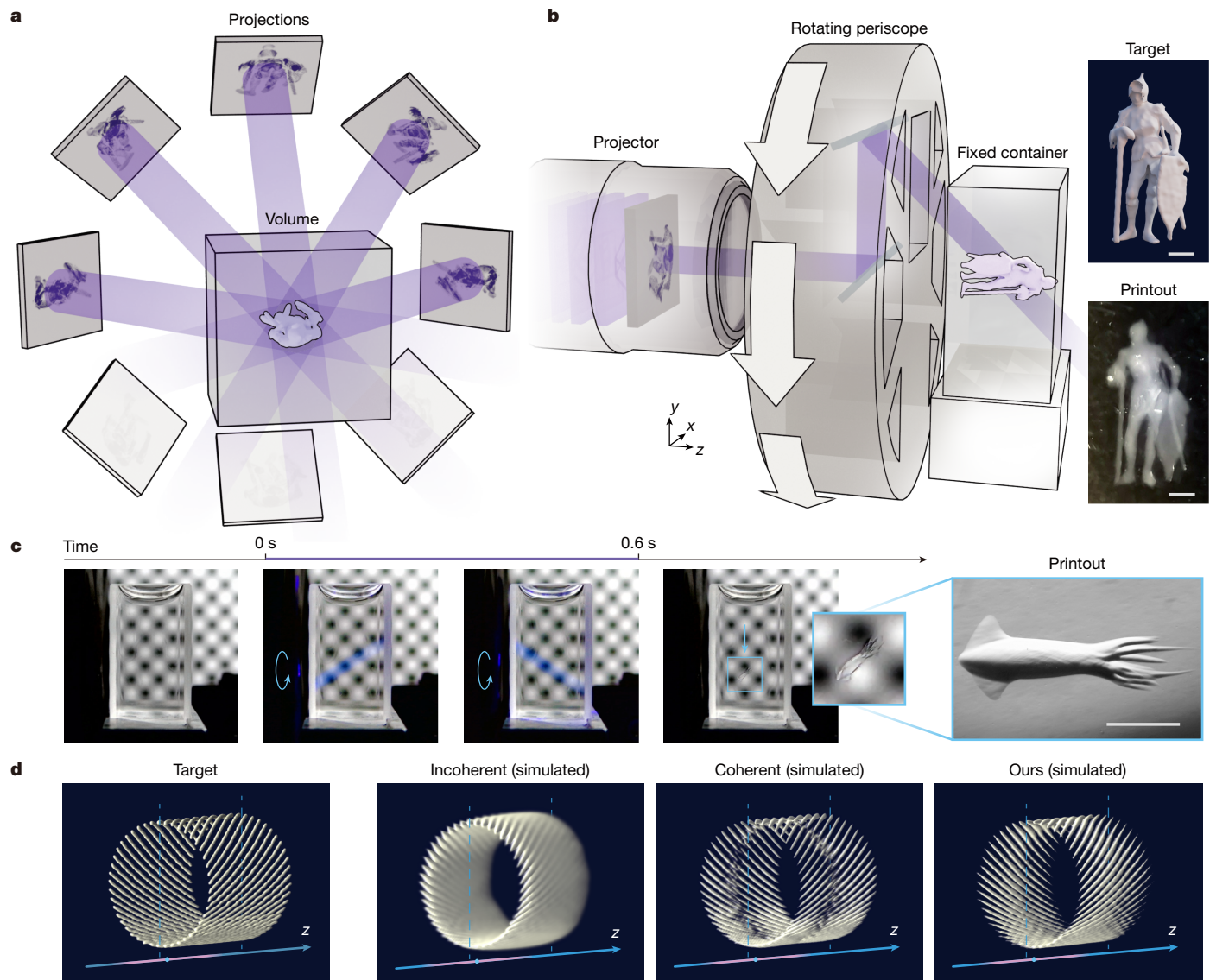


**Fig. 1 | Principle and illustration of DISH.** **a**, Multi-angle projection is used to generate 3D light intensity distributions within a fixed container for volumetric printing. **b**, A rotating periscope is designed to generate high-speed rotating projections of the light patterns modulated by a DMD within 0.6 s. The target model and its experimental printout are shown on the right as an example. **c**, Images captured at different time points showing that the printing process

in a low-viscosity PEGDA aqueous solution can be finished within 0.6 s.

**d**, Comparisons of the simulated 3D light distributions generated by the DISH system with incoherent light, coherent light without holographic optimization and coherent light with holographic optimization. The target ground truth is also shown on the left. Scale bars, 1 mm.

propagation model and a customized loss function to optimize the projected light fields holographically for high-resolution 3D modulation with enhanced fidelity compared with traditional algorithms. With substantially increased rotating speed and resolution over traditional CAL methods, DISH becomes very sensitive to system errors such as system misalignment, aberration and attenuation. Therefore, we develop an adaptive-optics-based rapid calibration method to achieve a uniform optical resolution of 11  $\mu\text{m}$  across 1-cm depth experimentally, enabling high-speed production of samples with the finest positive feature of 12  $\mu\text{m}$  and a stable printing resolution of 19  $\mu\text{m}$  (Extended Data Fig. 1). Different materials in a range of viscosities are validated to be compatible with DISH. By using both advantages of high efficiency and high precision, we integrate DISH with a fluidic channel to demonstrate successive flexible production of complex and diverse 3D structures within low-viscosity materials, which may open up a horizon for diverse applications such as high-throughput bioprinting, drug screening, micromachines and miniaturized photonics.

## Principle of DISH

To avoid the instability of high-speed sample rotation in traditional CAL methods, we develop a rotating periscope in DISH to facilitate high-speed projections of light fields at up to 10 rotations  $\text{s}^{-1}$  (Fig. 1a,b and Extended Data Fig. 2). A DMD is used to generate high-resolution light modulation at speeds up to 17,000 Hz. The periscope is placed in front of the objective, altering the propagation direction of patterned beams. The DMD patterns are synchronized accurately with the rotation angles for incoherent synthesis of 3D light intensity distributions (Extended Data Fig. 3). By rapidly changing the illumination angles, DISH makes use of the motor's rotation speed as the primary determinant of exposure time. All beams are projected through the single flat surface of a container to generate 3D patterns, simplifying requirements on the printing container and facilitating applications such as *in situ* printing on specific objects or *in vivo* bioprinting. Our experimental validation reveals that DISH can finish the 3D printing of a millimetre-scale object

within only 0.6 s in a polyethylene glycol diacrylate (PEGDA) aqueous solution (Fig. 1c and Supplementary Video 1). In traditional CAL methods, high-viscosity (6,000–10,000 cP) photosensitive materials are required to alleviate the effect of product sinking<sup>32</sup> owing to the printing time lasting tens of seconds. The ultrahigh printing speed of DISH can effectively mitigate these limitations and work for low-viscosity materials of 4.7 cP, accomplishing printing before sample sinking.

To further increase the printing resolution, we use a long-working-distance objective lens with a 0.055 NA for light projection. However, with the increase in resolution, the diffraction effect of light cannot be ignored by simply using the ray approximation. For partially coherent or incoherent light typically used in previous CAL methods, axial scanning will be required to cover a large volume range owing to the shallow depth of field with a high NA (about 0.4 mm for 0.055 NA at 405 nm), which will reduce the printing speed for millimetre-scale objects to maintain high resolution (Fig. 1d). In DISH, we address this problem by using a coherent laser source and holographically calculating and optimizing the light fields, which can achieve high-resolution modulation far beyond the native objective plane without mechanically shifting the focal plane. Combined with the high-speed digital modulation of the DMD, we can achieve high-resolution 3D light modulations across a large depth range up to 1 cm after specifically designed optimization, more than 20 times larger than the depth of field. Multi-angular excitation also offers sufficient degrees of freedom to generate high-resolution 3D intensity distributions by DMD modulation during optimization.

## Holographic light fields optimization

Different from the optimization process in CAL methods<sup>33–38</sup> using ray approximations for the light field, a coarse-to-fine iterative algorithm is developed for DISH to optimize the binary projection patterns in the DMD using the wave-optics model for coherent light. The projection patterns for different angles are summed incoherently to generate the 3D high-resolution intensity distributions for high-fidelity printing after considering the response of the photocuring materials<sup>39</sup>, which can be expressed as the following optimization problem:

$$\begin{aligned} \min \quad & L = \sum_{\vec{x} \in A} |d_h - D(\vec{x})|^2 + \sum_{\vec{x} \in \tilde{A}} |D(\vec{x}) - d|^2 \\ \text{s.t.} \quad & I = \sum_{\varphi} |\mathcal{H}_{\varphi}(\delta_{\varphi} u)|^2, \quad \delta_{\varphi} \in \{0, 1\} \end{aligned}$$

in which  $D(\vec{x})$  represents the accumulated dose at each 3D point in the objective area, which is determined by the intensity of the patterned beams  $I$ , exposure time and light attenuation in materials.  $A$  represents the 3D region of the target model to be printed, in which the accumulated dose is expected to be  $d_h$  for polymerization, and  $\tilde{A}$  represents the area outside the target region in which the accumulated dose is supposed to be smaller than the threshold  $d_l$  to avoid overexposure.  $\delta_{\varphi} u$  is the DMD-projected amplitudes for the angle  $\varphi$ .  $\mathcal{H}_{\varphi}$  represents the process of light propagation in wave optics, considering the refraction at the interface of air and material. By minimizing the loss function, we can optimize the binary projection patterns to achieve precise 3D intensity distributions and improve the printing accuracy (Methods).

Because such a binary discrete optimization problem involving more than 0.1 billion voxels for a millimetre-scale object is very time-consuming, we develop a coarse-to-fine iterative algorithm to reduce the computational costs (Fig. 2a). We first optimize this problem by existing gradient descent algorithms<sup>33,34</sup> to obtain high-resolution 3D intensity distributions  $I_{\varphi}^{\text{coarse}}$  for  $N$  discrete angles with the same 2D distributions along the angle  $\varphi$ . Then we use the synthesis of  $G$  adjacent binary projection patterns around the angle  $\varphi$  as a group. These groups for each angle are sequentially optimized through a holographic iterative algorithm (Methods) to fit the target high-resolution intensity distributions  $I_{\varphi}^{\text{coarse}}$  across a large depth range without the requirement

of mechanically shifting the focal plane. The flow chart of the holographic optimization is demonstrated in Extended Data Fig. 4, illustrating the necessity of holographic optimization for high-contrast 3D projections.

Compared with previous penalty minimization (PM) methods with ray approximation used in CAL<sup>33</sup>, our method can fully exploit the advantage of a coherent light source for holographic light fields to generate high-resolution 3D structures across about a 1-cm depth range for the 0.055-NA objective (Fig. 2b,c). We also compared our method with the global Gerchberg–Saxton algorithm<sup>40</sup>, a traditional iterative method for holographic pattern optimization. Our method achieves a more accurate intensity distribution in terms of the Jaccard index and signed distances, as shown in Fig. 2d and Extended Data Fig. 5. We further analysed the influence of the total number of projection patterns and the binarization parameter  $G$  on the printing accuracy. More projections will increase the printing fidelity and generally converge with more than 1,000 binary projections for different  $G$ . Our DMD can rapidly project 1,000 patterns within 0.06 s to ensure high printing speed. Although a smaller binarization parameter  $G$  can reach convergence with fewer projections, it leads to the loss of overall greyscale information with lower fidelity (Fig. 2e and Extended Data Fig. 6). The performance gradually converges when  $G$  is larger than 3. Therefore, we choose  $G = 10$  and a total projection number of 1,800 projections (corresponding to 180 coarse 3D doses) in practical experiments.

## Experimental calibration of DISH

We built up a proof-of-concept system to experimentally validate the performance of DISH. With both improvements in the printing speed and resolution, DISH is much more sensitive than previous CAL methods to system errors such as slight system misalignment, optical aberrations and beam attenuation. Therefore, careful calibration of the system is critical to achieve high performance experimentally. As depicted in Extended Data Fig. 7, the beam undergoes refraction at the surface between the air and the material during propagation. The pattern of the beam will be non-uniformly modulated after the refraction process, leading to blurring at the edge (Fig. 3a). Therefore, we took this refraction process into consideration during the wave-optics model of the beam propagation in the optimization algorithm to reduce errors (Methods).

Also, DISH is a non-coaxial, multi-view optical system. During the rotation of the periscope, any mismatch in different angular projections will lead to blurring of the integrated intensity, akin to the non-uniform optical aberrations. Therefore, we developed an adaptive-optics-based calibration method to calibrate the projection of each angle at the single-pixel level and ensure that all inclined beams precisely overlap at target positions. Inspired by digital adaptive optics in scanning light-field imaging<sup>41,42</sup>, the light intensity was first captured in the fluorescent material by two cameras placed in orthogonal directions, which worked as the wavefront sensors to detect the degrees of misalignment (Fig. 3b). Then we can laterally shift the projection patterns for each angle in the DMD using the measured misalignment as the feedback (Extended Data Fig. 8). By rotating the periscope and capturing the images of the beams for each angle, we can sequentially calibrate each angular projection based on the relationship among the DMD pixels, platform angles and 3D positions. Moreover, wave-optic parameters, such as the propagation distance to the native focal plane of the DMD, were calibrated by projecting designed stripes (Fig. 3c). The entire calibration process can be finished within a few minutes and only requires being carried out once for a fixed DISH system without the requirement of any hardware modifications. Accurate 3D intensity distributions for printing can then be achieved experimentally after both pattern optimization and adaptive-optics-based system calibration (Fig. 3d).

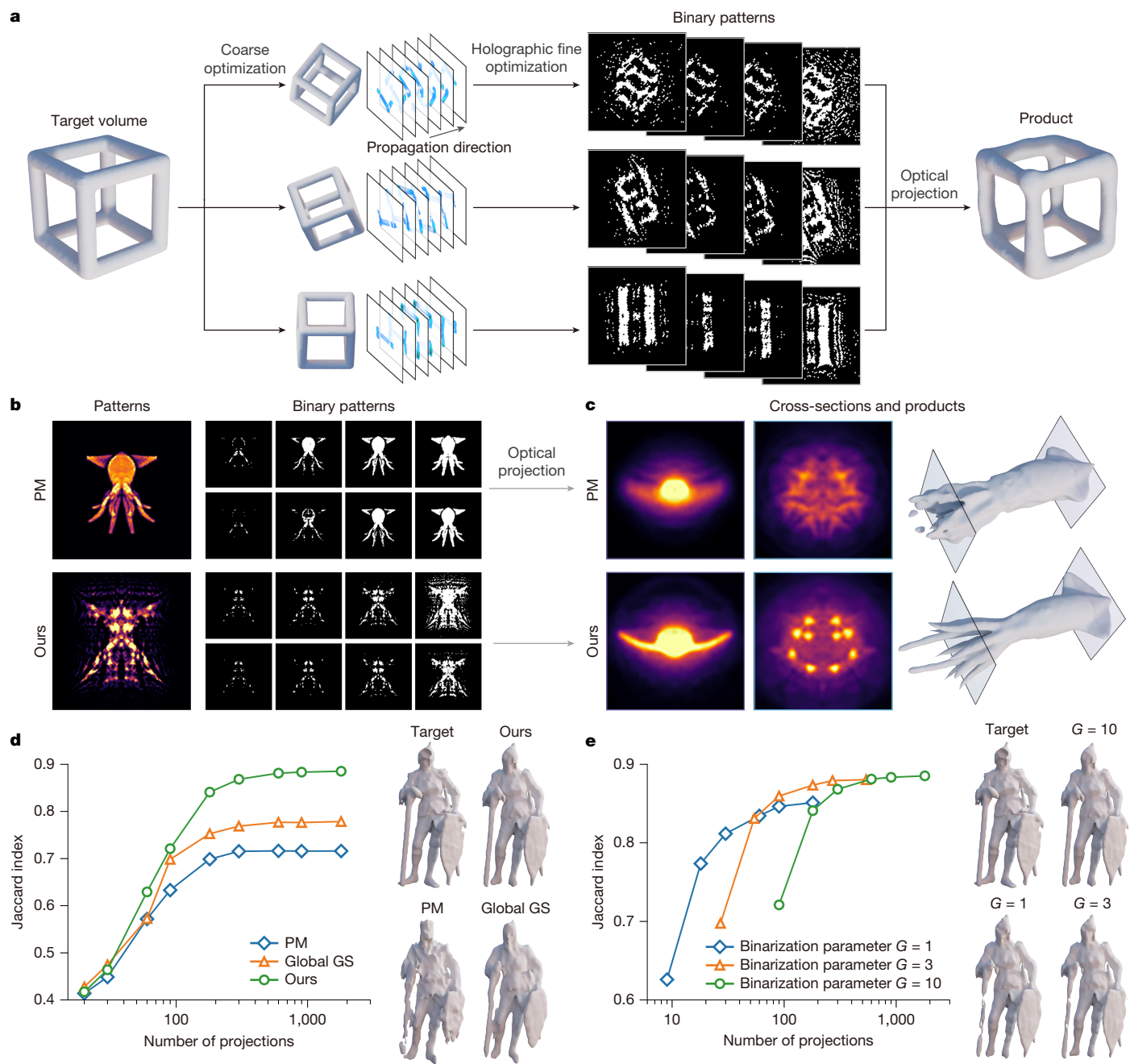


**Fig. 2 | Illustration and evaluations of the coarse-to-fine holographic optimization algorithm for the projection patterns.** **a**, Diagram illustrating the holographic optimization algorithm for multi-angle projections. An iterative holographic algorithm is developed to optimize binary patterns for each angle. **b**, Comparisons of the optimized patterns by the traditional PM algorithm and our holographic optimization algorithm. **c**, Simulated products and the cross-sections obtained by PM and our method. **d**, Curves of the Jaccard index

between the simulated products and the target versus the number of total binary projection patterns for each rotation round. The curves of three different methods were compared, including the PM algorithm, the global Gerchberg–Saxton (GS) algorithm and our algorithm. **e**, Curves of the Jaccard index between the simulated products and the target versus the number of total binary projection patterns for each rotation round. Curves of our method with different binarization parameters are shown.

To characterize the optical resolution of DISH quantitatively, we first imaged the 3D projection intensity generated by DISH in a fluorescent solution, with the exposure time of the cameras set as exactly the rotation time required for 360°. As shown in Fig. 3e,f, we projected the patterns of triple dots, each with a feature size and lateral spacing of 10.8 μm corresponding to two DMD pixels, at different axial positions with an axial interval of 2.4 mm. Although patterns optimized by backprojection and our method both successfully generated high-resolution structures at the printing centre near the focal plane, the backprojection method degraded at the axial position of 4.8 mm

from the printing centre owing to the defocus effect. By contrast, our method maintained high-resolution features even at the out-of-focus plane (<0.4 mm depth of field for a 0.055-NA objective) after holographic optimization (Fig. 3f).

### High-resolution 3D printing by DISH

To comprehensively evaluate the experimental printing resolution of DISH, we used DISH to print diverse sample structures. First, we printed high-resolution stripes on the 3D surface to evaluate the resolution

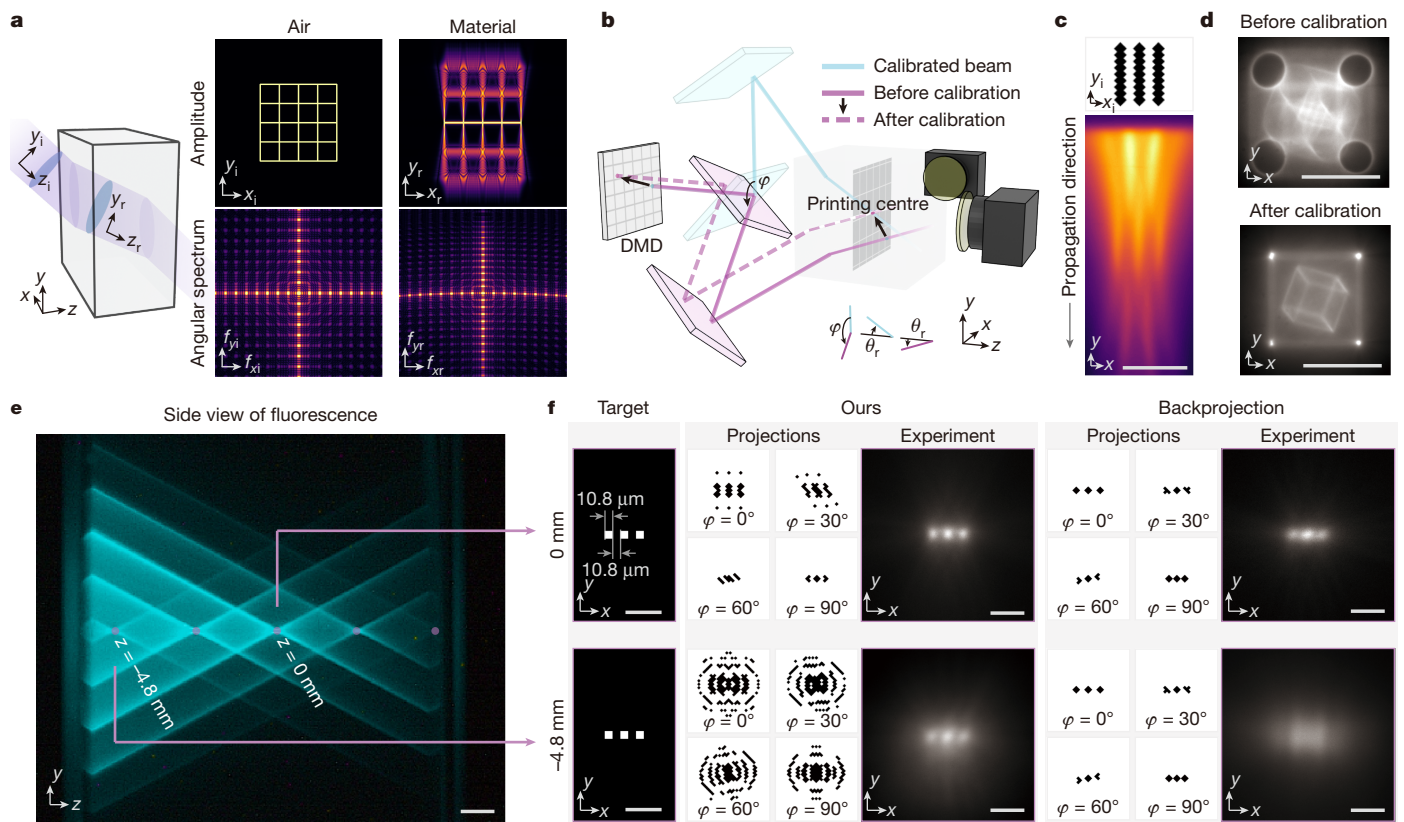


**Fig. 3 | Experimental calibration of DISH.** **a**, Illustration of the influence of the refraction at the interface of air and material by showing the amplitude and angular spectra before and after refraction. **b**, Schematic illustrating the adaptive-optics-based calibration process by updating the optimized patterns on the DMD for each angle based on fluorescence images captured by two orthogonal cameras. **c**, The beam projected from  $\varphi = 0^\circ$ , captured by the front camera, which helps determine the position of the conjugate plane. The image has been compressed in the vertical direction approximately ten times. **d**, Experimental fluorescence images of two cubes generated by DISH

before and after calibration. **e**, Experimental fluorescence images of beams focused at several axial positions across the printing area with an axial interval of 2.4 mm. **f**, Experimental fluorescence images of three dots with a designed feature size of 10.8  $\mu\text{m}$  and a gap of 10.8  $\mu\text{m}$ , located at the printing centre (upper row) and 4.8 mm away from the printing centre (bottom row). The ground-truth target is shown in the first column. Results obtained by two different optimization methods (our holographic optimization algorithm and backprojection) are shown with the corresponding optimized patterns for several angles on the left. Scale bars, 100  $\mu\text{m}$  (c); 1 mm (d,e); 50  $\mu\text{m}$  (f).

at different axial positions. A model with an axial length of 1 cm was designed with featured lines of different widths on the surface, with the smallest linewidth of 10.8  $\mu\text{m}$  corresponding to two DMD pixels (each pixel corresponds to about 5.4  $\mu\text{m}$  at the objective plane). Such a relief-structure model is particularly sensitive to dose contrast, making it suitable to evaluate overall projection precision. It should be noted that better resolution may be obtained if we use a DMD with a smaller pixel size and a larger pixel number, as a NA of 0.055 corresponds to a diffraction limit of about 3.68  $\mu\text{m}$  at 405 nm. The printed results are illustrated in Fig. 4a,b and the linewidth was measured as  $11.0 \pm 1.2 \mu\text{m}$  across the whole depth range. By contrast, the product generated by ray-approximation backprojections (Fig. 4c) showed much lower resolution away from the printing centre, indicating the shallow depth of field for the 0.055-NA excitation. Therefore, DISH with coherent light and holographic optimization enables high printing precision across 1 cm, more than 20 times larger than the depth of field of a NA of 0.055. Another sample covered with dense stripes was also printed to verify the resolution stability at different regions (Fig. 4d-f). Furthermore, we quantitatively measured the linewidths across different axial positions in the sample of Fig. 4a to validate the uniform resolution of DISH for millimetre-scale objects (Fig. 4g).

Then we tested the printing resolution on independent positive features. A fishbone model with a designed linewidth of 10.8  $\mu\text{m}$  was printed (Fig. 4h). The measured width after printing was  $11.9 \pm 2.1 \mu\text{m}$  (mean  $\pm$  standard deviation) across different bones at different regions

(Fig. 4i). High experimental printing resolution can also be visualized by the sharp edges and angles of the structures. Therefore, we used DISH to print the star (Fig. 4j) and the triangular pyramid (Fig. 4k). The designed angle of the star was  $36^\circ$  and the measured angles for different regions were about  $36.0 \pm 1.6^\circ$ , validating the high printing precision. To further validate the uniform printing resolution across the complete 3D volume and directions, we printed a conch model including lines aligned in different directions and axial positions (Fig. 4l-o). The linewidths after printing were measured as  $19.3 \pm 3.4 \mu\text{m}$ , indicating an overall uniform printing resolution of about 19  $\mu\text{m}$  for DISH on diverse positive structures. Similar uniform printing performance was validated by printing periodic structures across a large volume or a curved surface (Extended Data Fig. 9b-e). Negative features are more challenging for volumetric printing methods. We printed an inner conical model to show the versatility of DISH on diverse structures. The diameters of the inscribed circle were measured to be about 50  $\mu\text{m}$  (Extended Data Fig. 9f,g). Finally, we printed a complicated structure of a Theodoric statue and validated our printing fidelity by comparing the designed model with the scanning results by X-ray computed tomography on our printed product (Extended Data Fig. 9h).

## High-speed successive 3D printing

By increasing both the printing speed and precision of millimetre-scale samples with volumetric exposure, DISH facilitates mass production

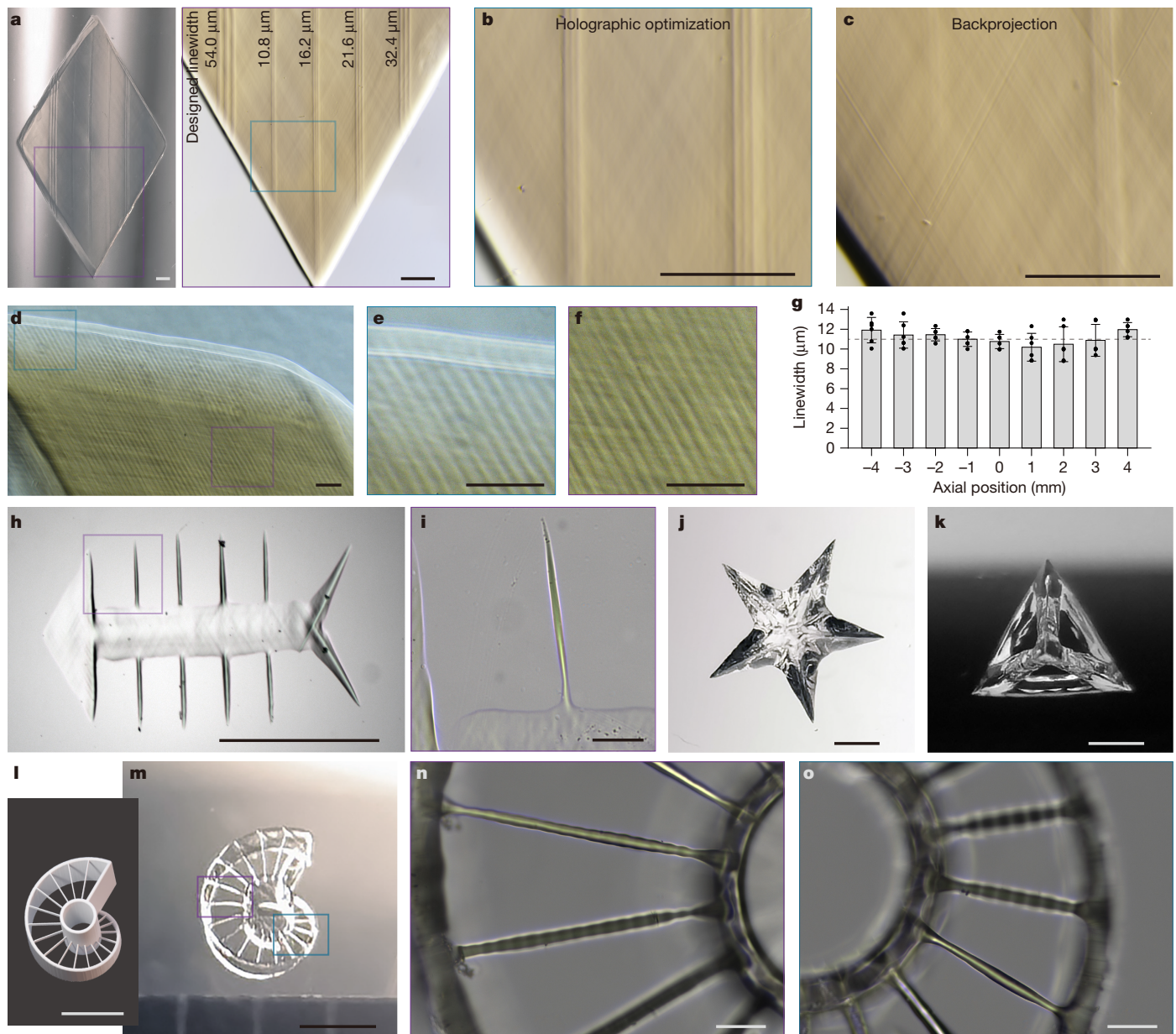


**Fig. 4 | Experimental characterization of the printing resolution of DISH.** **a**, Relief-structure products printed by DISH, demonstrating the smallest feature size over a 1-cm range. The linewidths were measured as  $54.0 \pm 2.9$ ,  $11.0 \pm 1.2$ ,  $15.5 \pm 1.9$ ,  $20.9 \pm 2.3$  and  $33.1 \pm 2.1 \mu\text{m}$ , respectively. **b**, Close-up view of the relief structure printed using patterns optimized by our holographic optimization algorithm. **c**, Close-up view of a relief structure printed using patterns optimized by the conventional ray-optic backprojection algorithm. **d**, Relief-structure sample with dense stripes printed by DISH. **e,f**, Close-up images of the edge (**e**) and middle (**f**) regions of the sample in **d**. **g**, Average linewidths measured at different axial positions of the sample in **a**, demonstrating a uniform resolution of  $11 \mu\text{m}$  over a 1-cm depth range. We used  $n = 6$  measurements for each position,

with error bars representing the standard deviation. **h,i**, Fishbone structure and its close-up view printed by DISH, in which its positive features were measured to be  $11.9 \pm 2.1 \mu\text{m}$ . **j**, Five-pointed star model with designed angles of  $36^\circ$  and measured angles of  $36.0 \pm 1.6^\circ$ . **k**, Triangular pyramid with sharp edges. **l–o**, Conch model (**l**) and the printout result by DISH (**m**). The lines aligned in different directions and z-axis positions were measured to be  $19.3 \pm 3.4 \mu\text{m}$  (**n,o**). As the lines are distributed along the z-axis positions, those located outside the microscope focal plane appear as defocused patterns. We used mean  $\pm$  standard deviation here for the width measurement. Scale bars,  $500 \mu\text{m}$  (**a–c**);  $200 \mu\text{m}$  (**d–f**);  $1 \text{ mm}$  (**h,j–m**);  $100 \mu\text{m}$  (**i,n,o**).

of diverse 3D structures, which is critical for practical applications such as high-throughput drug screening<sup>43</sup>, mass fabrication of photonics computing devices<sup>44</sup> and bioprinting<sup>45</sup>. To demonstrate this advantage, we integrated DISH with a fluidic channel for high-speed mass 3D printing (Fig. 5a). A pump was used to shift the products and replenish the printing material and a strainer was used to collect the printing products while separating the uncured material for reuse. The exposure time of each sample was 0.6 s (Supplementary Video 2). Different from traditional mass production methods with a fixed mould

for the same structure, DISH can successively manufacture different objects with both high efficiency and high flexibility (Fig. 5b,c).

For industrial or engineering applications, we demonstrated intricate shapes with complicated surfaces and hanging structures such as the Theodoric statue (Fig. 5d,e), the squid (Fig. 5f) and the Benchy (Fig. 5g), among others (Extended Data Fig. 9). For biological applications, we demonstrated helical tubes to mimic the vessels (Fig. 5h and Extended Data Fig. 9i). The hollow structure was validated by injecting different colours of ink. Because the light is only projected from one

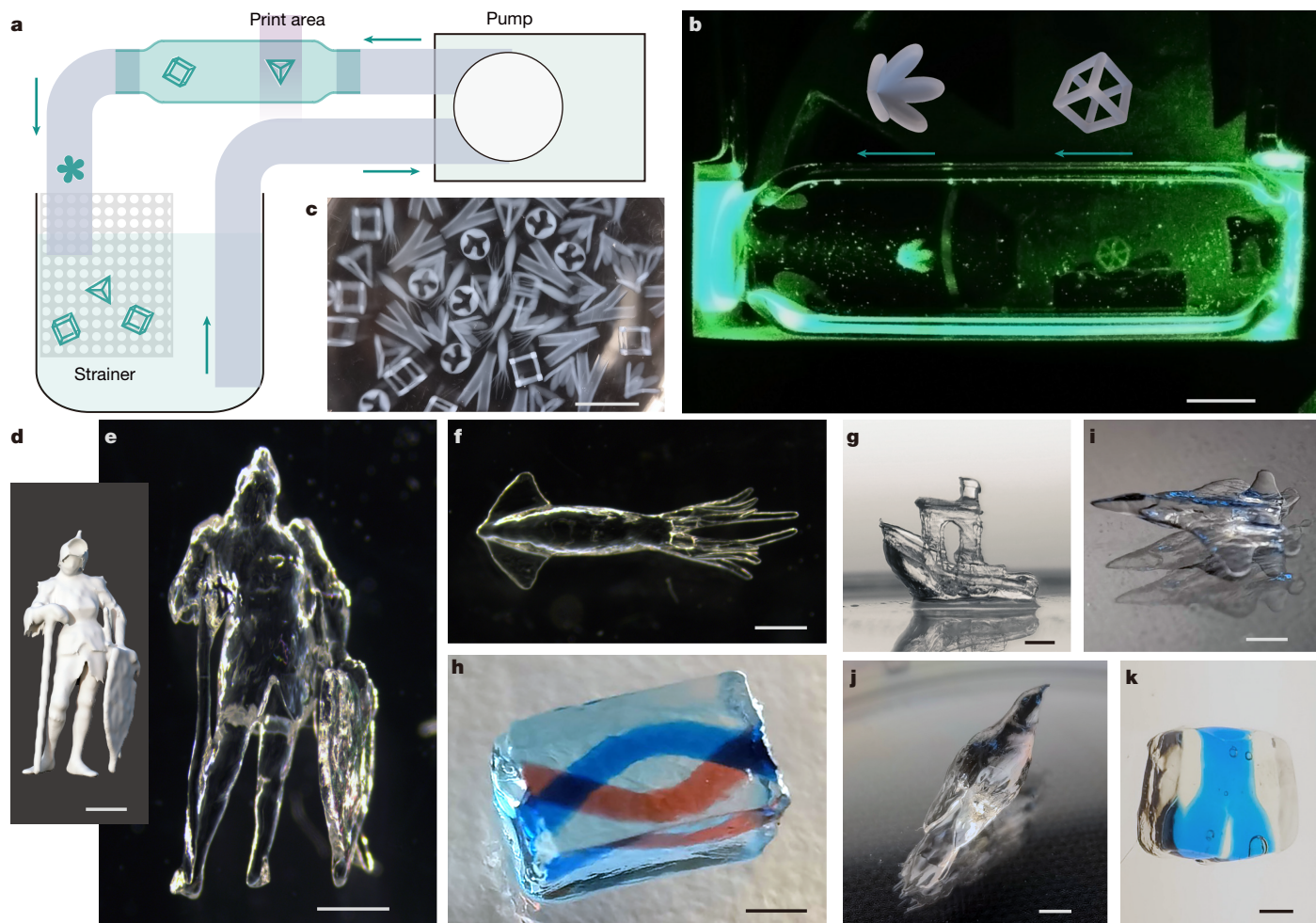


**Fig. 5 | Successive 3D printing of diverse structures by DISH with a fluidic channel.** **a**, Schematic illustrating DISH integrated with a fluidic channel, a pump and a strainer for mass production and collection of printouts in flow. **b**, Photographs depicting the printing process in flow. **c**, Diverse structures printed at high speed by DISH, including cube frames, tetrahedron frames, flowers, squids, spinal cord slices and bifurcated tubes. **d,e**, Digital model (**d**) and PEGDA printed product (**e**) of the Theodoric statue. **f**, Squid statuette printed with PEGDA. **g**, Benchy model printed with PEGDA. **h**, Helical tubes as common models in biological applications. Red and blue dyes were injected for visualization. **i**, Airplane printed with DPHA. **j**, Bird printed with BPAGDA. **k**, Bifurcated tube printed with soft biomaterial GelMA. Scale bars, 5 mm (**b,c**); 1 mm (**d–k**).

and PEGDA printed product (**e**) of the Theodoric statue. **f**, Squid statuette printed with PEGDA. **g**, Benchy model printed with PEGDA. **h**, Helical tubes as common models in biological applications. Red and blue dyes were injected for visualization. **i**, Airplane printed with DPHA. **j**, Bird printed with BPAGDA. **k**, Bifurcated tube printed with soft biomaterial GelMA. Scale bars, 5 mm (**b,c**); 1 mm (**d–k**).

side by DISH, intravital *in situ* bioprinting of diverse structures on a fixed surface can be conducted at high speed. Also, because the entire 3D volume is printed simultaneously, DISH enables the printing of unsupported chains, which are challenging for extrusion or layer-wise printing techniques (Extended Data Fig. 9j).

Also, DISH is a general framework that can be compatible with common 3D printing materials. We further demonstrated the application of several frequently used photocuring materials in DISH. The rigid structures printed with dipentaerythritol hexaacrylate (DPHA) and bisphenol A glycerolate (1 glycerol/phenol) diacrylate (BPAGDA) were demonstrated in Fig. 5i,j and Extended Data Fig. 9n. Tubes were also printed with biomolecule-based hydrogels gelatin methacrylate (GelMA) and silk fibrin methacryloyl (SilMA) (Fig. 5k and Extended Data Fig. 9o). Moreover, elastic materials such as urethane dimethacrylate (UDMA) can also be printed, as shown in Extended Data Fig. 9p. All of these experiments demonstrate the broad applications of DISH with both high flexibility and efficiency.

## Discussion

In summary, we introduce a volumetric 3D printing method, DISH, capable of successively producing high-resolution, millimetre-scale

objects within 0.6 s. With the integration of a series of developments in both hardware and software, the system can be calibrated within several minutes without further hardware modification, achieving a uniform printing resolution of about 19- $\mu$ m feature size across the 1-cm range throughout the container experimentally.

In additive manufacturing, higher spatial resolution or smaller voxel size results in a substantial increase in the number of voxels required per unit volume, which consequently decreases volumetric build rate. Conversely, enhancing volumetric build rate often occurs at the cost of reduced resolution. Voxel printing rate is therefore a parameter that enables intuitive characterization of 3D printing efficiency across several length scales. Using DISH, a sample with a volume of approximately 200 mm<sup>3</sup> (Extended Data Fig. 2e) can be produced in a minimum exposure time of 0.6 s, achieving a volume printing rate of 333 mm<sup>3</sup> s<sup>-1</sup> and a voxel printing rate of  $1.25 \times 10^8$  voxels s<sup>-1</sup> at a voxel size of  $(11 \mu\text{m})^3 \times 22 \mu\text{m}$  (Extended Data Fig. 8e). Compared with other 3D printing methods, DISH shows great improvement in speed and resolution when manufacturing millimetre-scale samples (Extended Data Fig. 1). In the future, the DMD and the rotation periscope can reach a much faster speed up to 10 rotations s<sup>-1</sup> to further accelerate the build rate, as long as a laser source with higher power is used. Furthermore, the batch processing speed in the fluidic system

is expected to be improved once rapid and stable switching between flowing and static states is realized through precise flow control. As for the computational cost of the algorithm before the printing process, DISH is comparable with other computed holographic methods<sup>31</sup>. Still, after acquiring high-resolution datasets that account for refractive aberrations, introducing end-to-end neural networks for 3D hologram generation<sup>46,47</sup> and graphics processing unit (GPU) acceleration may greatly reduce the computational cost.

Various factors influence the experimental printing resolution, such as the projection methods, the non-linear response of the materials and the structures of target products. High-precision dose distributions of 11  $\mu\text{m}$  have been observed in fluorescent solutions and relief-structure printouts of DISH (Figs. 3f and 4a,b). However, our experiments, along with relevant literature<sup>29</sup>, indicate that isolated small structures require much higher dose contrast and are sensitive to the surrounding dose distribution, highlighting the need for more precise dose control. At present, we have achieved about 19  $\mu\text{m}$  overall printing resolution across the effective depth range and 12  $\mu\text{m}$  as the finest independent positive feature (Fig. 4). Algorithms that can increase dose contrast or take diffusion into consideration may further improve the overall printing resolution near the optical diffraction limit. Besides, a DMD with a larger pixel number and smaller pixel size can further improve the printing throughput with either a larger field of view or a higher printing resolution. Another factor reducing product quality is speckle noise, which causes intensity inhomogeneities and stripe-like artefacts along the beam propagation direction. The traditional perpendicular projection causes stripes to overlap, forming transverse patterns. By contrast, our inclined projection system avoids this issue, resulting in less prominent stripes. Nonetheless, the surface quality could be further improved by using several or tiled holograms to suppress speckle noises or introducing beam translation by means of optical components.

The proposed design of single-side illumination enables *in situ* printing but introduces the missing-cone problem, slightly reducing the axial resolution compared with the lateral resolution. Changing the mechanical design of the periscope can address this problem (Extended Data Fig. 10). However, the substantial variation in propagation direction for curved container surfaces violates the paraxial approximation required for angular spectrum modelling, in which an extremely high spatial sampling frequency is needed to model the phase modulation process induced by the curved surface during calculation. Consequently, higher computational costs would be required and both aberrations and depth of field should be re-evaluated to ensure the resolution of printed structures in this case.

As well as the mass production of diverse samples by integrating DISH with a fluidic device, more applications can be explored in the future. Direct *in situ* printing in pipelines and Petri dishes can be applied in biology for high-throughput drug screening. Massive printing in a steady multi-material laminar flow can be realized with specialized fluidics<sup>24,48</sup>. Photonic computing devices and diverse imaging systems, such as the camera module in mobile phones, may be fabricated at high throughput with DISH. With both high precision and high efficiency, we believe that DISH may open up a horizon for broad applications with ultrahigh-speed 3D printing, including biology, photonics and engineering.

## Online content

Any methods, additional references, Nature Portfolio reporting summaries, source data, extended data, supplementary information, acknowledgements, peer review information; details of author contributions and competing interests; and statements of data and code availability are available at <https://doi.org/10.1038/s41586-026-10114-5>.

1. Kelly, B. E. et al. Volumetric additive manufacturing via tomographic reconstruction. *Science* **363**, 1075–1079 (2019).

2. Bernal, P. N. et al. The road ahead in materials and technologies for volumetric 3D printing. *Nat. Rev. Mater.* **10**, 826–841 (2025).
3. Dudukovic, N. A. et al. Cellular fluidics. *Nature* **595**, 58–65 (2021).
4. Zheng, X. et al. Multiscale metallic metamaterials. *Nat. Mater.* **15**, 1100–1106 (2016).
5. Feng, S. et al. Three-dimensional capillary ratchet-induced liquid directional steering. *Science* **373**, 1344–1348 (2021).
6. Thiele, S., Arzenbacher, K., Gissibl, T., Giessen, H. & Herkommer, A. M. 3D-printed eagle eye: compound microlens system for foveated imaging. *Sci. Adv.* **3**, e1602655 (2017).
7. Luo, Z., Cerejon, D. K., Römer, S., Zoratto, N. & Leroux, J.-C. Boosting systemic absorption of peptides with a bioinspired buccal-stretching patch. *Sci. Transl. Med.* **15**, eabq1887 (2023).
8. Catarino, C. M., Schuck, D. C., Dechiaro, L. & Karande, P. Incorporation of hair follicles in 3D bioprinted models of human skin. *Sci. Adv.* **9**, eadg0297 (2023).
9. Vidler, C. et al. Dynamic interface printing. *Nature* **634**, 1096–1102 (2024).
10. Mazzocchi, A., Soker, S. & Skardal, A. 3D bioprinting for high-throughput screening: drug screening, disease modeling, and precision medicine applications. *Appl. Phys. Rev.* **6**, 011302 (2019).
11. Fernandes, C., Pontes, A. J., Viana, J. C. & Gaspar-Cunha, A. Modeling and optimization of the injection-molding process: a review. *Adv. Polym. Technol.* **37**, 429–449 (2018).
12. Marre, S. & Jensen, K. F. Synthesis of micro and nanostructures in microfluidic systems. *Chem. Soc. Rev.* **39**, 1183–1202 (2010).
13. Melchels, F. P., Feijen, J. & Grijpma, D. W. A review on stereolithography and its applications in biomedical engineering. *Biomaterials* **31**, 6121–6130 (2010).
14. Ahn, D., Stevens, L. M., Zhou, K. & Page, Z. A. Rapid high-resolution visible light 3D printing. *ACS Cent. Sci.* **6**, 1555–1563 (2020).
15. Dhand, A. P. et al. Additive manufacturing of highly entangled polymer networks. *Science* **385**, 566–572 (2024).
16. Grigoryan, B. et al. Multivascular networks and functional intravascular topologies within biocompatible hydrogels. *Science* **364**, 458–464 (2019).
17. Maruo, S., Nakamura, O. & Kawata, S. Three-dimensional microfabrication with two-photon-absorbed photopolymerization. *Opt. Lett.* **22**, 132–134 (1997).
18. Farsari, M. & Chichkov, B. N. Two-photon fabrication. *Nat. Photon.* **3**, 450–452 (2009).
19. Saha, S. K. et al. Scalable submicrometer additive manufacturing. *Science* **366**, 105–109 (2019).
20. Tumbleston, J. R. et al. Continuous liquid interface production of 3D objects. *Science* **347**, 1349–1352 (2015).
21. Walker, D. A., Hedrick, J. L. & Mirkin, C. A. Rapid, large-volume, thermally controlled 3D printing using a mobile liquid interface. *Science* **366**, 360–364 (2019).
22. Kronenfeld, J. M., Rother, L., Saccone, M. A., Dulay, M. T. & DeSimone, J. M. Roll-to-roll, high-resolution 3D printing of shape-specific particles. *Nature* **627**, 306–312 (2024).
23. Regehy, M. et al. Xolography for linear volumetric 3D printing. *Nature* **588**, 620–624 (2020).
24. Stuwe, L. et al. Continuous volumetric 3D printing: xolography in flow. *Adv. Mater.* **36**, 2306716 (2024).
25. Shusteff, M. et al. One-step volumetric additive manufacturing of complex polymer structures. *Sci. Adv.* **3**, eaao5496 (2017).
26. Bernal, P. N. et al. Volumetric bioprinting of complex living-tissue constructs within seconds. *Adv. Mater.* **31**, 1904209 (2019).
27. Bernal, P. N. et al. Volumetric bioprinting of organoids and optically tuned hydrogels to build liver-like metabolic biofactories. *Adv. Mater.* **34**, 2110054 (2022).
28. Toombs, J. T. et al. Volumetric additive manufacturing of silica glass with microscale computed axial lithography. *Science* **376**, 308–312 (2022).
29. Orth, A. et al. Deconvolution volumetric additive manufacturing. *Nat. Commun.* **14**, 4412 (2023).
30. Loterie, D., Delrot, P. & Moser, C. High-resolution tomographic volumetric additive manufacturing. *Nat. Commun.* **11**, 852 (2020).
31. Wechsler, F., Gigli, C., Madrid-Wolff, J. & Moser, C. Wave optical model for tomographic volumetric additive manufacturing. *Opt. Express* **32**, 14705 (2024).
32. Salajeghe, R., Meile, D. H., Kruse, C. S., Marla, D. & Spangenberg, J. Numerical modeling of part sedimentation during volumetric additive manufacturing. *Addit. Manuf.* **66**, 103459 (2023).
33. Bhattacharya, I., Toombs, J. & Taylor, H. High fidelity volumetric additive manufacturing. *Addit. Manuf.* **47**, 102299 (2021).
34. Rackson, C. M. et al. Object-space optimization of tomographic reconstructions for additive manufacturing. *Addit. Manuf.* **48**, 102367 (2021).
35. Orth, A. et al. On-the-fly 3D metrology of volumetric additive manufacturing. *Addit. Manuf.* **56**, 102869 (2022).
36. Chen, T. H. et al. High-fidelity tomographic additive manufacturing for large-volume and high-attenuation situations using expectation maximization algorithm. *Addit. Manuf.* **80**, 103968 (2024).
37. Orth, A., Sampson, K. L., Ting, K., Boisvert, J. & Paquet, C. Correcting ray distortion in tomographic additive manufacturing. *Opt. Express* **29**, 11037–11054 (2021).
38. Webber, D. et al. Versatile volumetric additive manufacturing with 3D ray tracing. *Opt. Express* **31**, 5531–5546 (2023).
39. O'Brien, A. K. & Bowman, C. N. Impact of oxygen on photopolymerization kinetics and polymer structure. *Macromolecules* **39**, 2501–2506 (2006).
40. Piestun, R., Spektor, B. & Shamir, J. Wave fields in three dimensions: analysis and synthesis. *J. Opt. Soc. Am. A* **13**, 1837–1848 (1996).
41. Wu, J. M. et al. Iterative tomography with digital adaptive optics permits hour-long intravital observation of 3D subcellular dynamics at millisecond scale. *Cell* **184**, 3318–3332 (2021).
42. Wu, J. et al. An integrated imaging sensor for aberration-corrected 3D photography. *Nature* **612**, 62–71 (2022).
43. Qu, J., Kalyani, F. S., Liu, L., Cheng, T. & Chen, L. Tumor organoids: synergistic applications, current challenges, and future prospects in cancer therapy. *Cancer Commun.* **41**, 1331–1353 (2021).

44. Chen, Y. et al. All-analog photoelectronic chip for high-speed vision tasks. *Nature* **623**, 48–57 (2023).
45. Lee, M., Rizzo, R., Surman, F. & Zenobi-Wong, M. Guiding lights: tissue bioprinting using photoactivated materials. *Chem. Rev.* **120**, 10950–11027 (2020).
46. Shi, L., Li, B., Kim, C., Kellnhofer, P. & Matusik, W. Towards real-time photorealistic 3D holography with deep neural networks. *Nature* **591**, 234–239 (2021).
47. Shi, L., Li, B. & Matusik, W. End-to-end learning of 3D phase-only holograms for holographic display. *Light Sci. Appl.* **11**, 247 (2022).
48. Pregibon, D. C., Toner, M. & Doyle, P. S. Multifunctional encoded particles for high-throughput biomolecule analysis. *Science* **315**, 1393–1396 (2007).

**Publisher's note** Springer Nature remains neutral with regard to jurisdictional claims in published maps and institutional affiliations.



**Open Access** This article is licensed under a Creative Commons Attribution-NonCommercial-NoDerivatives 4.0 International License, which permits any non-commercial use, sharing, distribution and reproduction in any medium or format, as long as you give appropriate credit to the original author(s) and the source, provide a link to the Creative Commons licence, and indicate if you modified the licensed material. You do not have permission under this licence to share adapted material derived from this article or parts of it. The images or other third party material in this article are included in the article's Creative Commons licence, unless indicated otherwise in a credit line to the material. If material is not included in the article's Creative Commons licence and your intended use is not permitted by statutory regulation or exceeds the permitted use, you will need to obtain permission directly from the copyright holder. To view a copy of this licence, visit <http://creativecommons.org/licenses/by-nc-nd/4.0/>.

© The Author(s) 2026

## Methods

### Experimental set-up

Extended Data Fig. 2 shows the experimental set-up of DISH. A coherent 405-nm light beam emitted from the continuous-wave diode laser CNI MDL-HD-405 with a linewidth of 1.5 nm is modulated by a DMD equipped with a total internal reflection prism. The DMD (TI DLP9500) driven by VIALUX V-9501 features a pixel size of 10.8  $\mu\text{m}$ , an array size of  $1,920 \times 1,080$  and a refresh rate of 17.9 kHz. The patterned beam passes through a 4f system, consisting of a tube lens (Thorlabs TTL200-A), an aperture and an objective lens with a working distance of 34 mm (Mitutoyo M Plan Apo 2 $\times$ , NA 0.055). The aperture allows only the central diffraction order to pass. The beam is then directed into a periscope fixed on a hollow rotating platform, driven by an alternating current servo motor (Panasonic MSMJ042G1U). Finally, the beam is obliquely projected into a quartz cuvette, with an entry maximum power density of 150 mW  $\text{cm}^{-2}$  and a total maximum power of 40 mW, limited by the laser. The periscope consists of two small mirrors (Extended Data Fig. 2c,d). The first mirror is inclined at a 45° angle relative to the  $z$ -axis and the second mirror is inclined at 22.5°. After reflection within the periscope, the beam is projected into the container at a 45° angle. When the incident angle is 45°, this configuration yields a reasonable axial feature size for most materials with different refractive indices, while keeping the interface reflectivity low. This mechanical design accommodates a light beam of 6 mm in diameter. As shown in Extended Data Fig. 2e, the printing area exhibits a centrally symmetric spindle-like shape, which can be approximated by a cylinder and two cones. The total volume of this approximated shape is  $\frac{1}{4}\pi d^3 \frac{1}{\tan\theta_r} \left( \frac{1}{\cos\theta_i} - \frac{2}{3} \right)$ , in which  $\theta_i$  represents the incident angle,  $\theta_r$  represents the refracted angle and  $d$  represents the beam diameter. When  $d = 5.832$  mm (5.4  $\mu\text{m} \times 1,080$ ) and the refractive index of the material is 1.48, the total volume is 214.1  $\text{mm}^3$ .

The time sequence diagram of the synchronization of rotation and the projection pattern is detailed in Extended Data Fig. 3. A National Instruments PCIe-6363 multifunction I/O device is used to generate voltage pulses and control various components, including the laser shutter, camera shutter, projection angle and DMD projections. The servo motor is operated at 1,000 rpm, resulting in a period of 0.6 s for the hollow rotating platform with a 1:10 reduction ratio. DMD projections are synchronized with the actual angle. During the printing process, the laser shutter is closed until the motor speed stabilizes. The shutter controls the exposure time to be 0.6 s. Typically, the servo motor is triggered with a 60-kHz square wave, whereas the DMD is triggered with a 3-kHz square wave, showing 1,800 projections per cycle. The running speed could also be adjusted as needed. Because the laser power used in our prototype system is relatively low, all trigger parameters described here are specifically configured for the 0.6-s exposure time rather than for maximum operating speed.

### Modelling of the system

The relationship between the beam propagation coordinates  $(x_r, y_r, z_r)$  and the world coordinates  $(x, y, z)$  is established to ensure compatibility with any 3D projection direction. The coordinates  $(x, y, z)$  are defined according to the container. The  $z$ -axis represents the rotation axis, the  $x$ -axis represents the horizontal direction and the  $y$ -axis represents the vertical direction. The coordinates  $(x_r, y_r, z_r)$  are defined according to the beam inside the container, with the  $z_r$ -axis indicating the propagation direction. Both coordinate systems share the same origin, which is the printing centre. In our experimental set-up, the coordinate transformation can be represented by the Euler angle representation:

$$(x, y, z)^T = R_z(\varphi)R_x(\theta_r)R_z(-\varphi) \cdot (x_r, y_r, z_r)^T$$

in which  $\varphi$  represents the platform angle and  $\theta_r$  represents the refraction angle in the material.  $R_x$  and  $R_z$  represent the rotation around the  $x$ -axis and  $z$ -axis, respectively.

In wave optics, the propagation is modelled as:

$$\begin{cases} \mathcal{H}_\varphi(z_r) = \mathcal{F}^{-1}H(z_r + l_r, \lambda_r) \cdot S_\varphi \cdot H(l_r, \lambda_r) \mathcal{F} \\ H(z, \lambda) = \exp\left\{j\frac{2\pi}{\lambda}z\sqrt{1 - (\lambda f_x)^2 - (\lambda f_y)^2}\right\} \end{cases}$$

Here  $\mathcal{F}$  denotes the Fourier transformation that converts complex amplitudes into angular spectra.  $H(l_r, \lambda_r)$  and  $H(z_r + l_r, \lambda_r)$  are the propagation matrices in air and in the material, respectively.  $S_\varphi$  represents refraction, which is achieved through a distorted stretching in the angular spectrum. As the plane wave remains a plane wave after refraction at a flat interface, the corresponding relationship of angular spectrum coordinates before and after refraction can be calculated using the 3D form of Snell's law. This distorted stretching on the angular spectrum is implemented by the `imwarp` function in MATLAB.

### Adaptive-optics-based calibration

To simplify the calibration process, the optical system preceding the periscope was adjusted to ensure that the beam emitted from the DMD centre precisely coincides with the rotation axis of the platform. Therefore, the rotating light path was adjusted to be centrosymmetric and the angle of incidence  $\theta_i$  remained unchanged. Owing to the symmetry of the system, the beam emitted from the DMD centre should generate intensity with the shape of a one-sheet hyperboloid within the container. Its symmetric centre was considered as the printing centre and the origin of the world coordinates. The distance from the printing centre to the front surface of the container was denoted as  $z_0$ . During calibration, the optical devices were fixed and only the projections were updated as the platform rotated.

First, a coarse linear relationship between the DMD pixel coordinates, platform angle and 3D coordinates inside the container was established. DMD pixels were activated individually while the platform was slowly rotating and the corresponding excited fluorescence in the container 18  $\mu\text{g ml}^{-1}$  coumarin-30 DMSO resolution was captured in real time by the front and side cameras equipped with emission filters. As illustrated in Extended Data Fig. 8b, the projection angle  $\varphi$  of the beam was determined using the front camera, whereas the angle of refraction  $\theta_r$  was measured with the side camera. The remaining two degrees of freedom of the ray were calculated by the position of its intersection point with the  $z = 0$  plane. The DMD pixel was then shifted according to the fluorescent photographs taken from the cameras. Finally, a set of DMD offset pixels that emitted beams to exactly intersect the printing centre was obtained, denoted by  $(x_i^{0\varphi}, y_i^{0\varphi})$ . Extended Data Fig. 8c,d show an example of the positions of the beam before and after calibration.

Subsequently, the propagation distance from the conjugate plane to the interface of the container was measured. When the platform angle  $\varphi = 0$ , line segments at the  $y$ - $z$  plane (Fig. 3c) were projected and the symmetrical centre of the resulting 3D intensity was considered as the approximate conjugate plane. Several images were captured at different focal planes with an electrotunable lens and the symmetric centre of their composite photograph identified the approximate conjugate plane of the DMD. The propagation distance from the printing centre to the approximate conjugate plane was denoted as  $z_r^c$ .

Finally, the precise calibration was operated with holographically synthesized patterns. The focusing performance throughout the container was checked and the calibrated parameters were fine-tuned until the intensities at all platform angles were consistent with the simulation of wave-optic propagation. When the container was shifted for a distance of  $z'$  along the  $z$ -axis and the material was replaced by that with a refractive index of  $n'$ , these parameters could be recalculated as follows without the requirement of extra calibration experiments:

$$\begin{aligned}
n' \sin \theta'_r &= n \sin \theta_r \\
z'_r \tan \theta'_r &= z_0 \tan \theta_r - z' \tan \theta_r \\
z'_r \sin \theta'_r &= z_r \sin \theta_r \\
(x_i^{0\phi'}, y_i^{0\phi'}) &= (x_i^{0\phi}, y_i^{0\phi})
\end{aligned}$$

## Holographic optimization algorithm

First, the optimization problem to obtain the coarse 3D intensity distributions  $I_\phi^{\text{coarse}}$  contributed by each angle is shown below:

$$\begin{cases} \min \quad L = \sum_{\vec{x} \in A} |d_h - \mu(\vec{x})I(\vec{x})\Delta t|^2 \\ \quad + \sum_{\vec{x} \in \tilde{A}} |\mu(\vec{x})I(\vec{x})\Delta t - d_l|^2, \\ \text{s. t.} \quad I = \sum_\phi I_\phi^{\text{coarse}} \end{cases}$$

in which  $\vec{x}$  represents the 3D coordinates in the objective area,  $\phi$  represents the projection angle,  $\mu(\vec{x})$  represents the attenuation during the propagation in materials and thus  $\mu(\vec{x})I(\vec{x})\Delta t$  represents the accumulated dose at each point.  $A$  represents the 3D region of the target model to be printed, in which the accumulated dose is expected to be  $d_h$  for polymerization and  $\tilde{A}$  represents the area outside the target region in which the accumulated dose is supposed to be smaller than the threshold  $d_l$  to avoid overexposure.  $\Delta t$  corresponds to the temporal duration of each projection. The number of projection angles for optimization in this step can be reduced by duplicating the pattern with adjacent angles to accelerate the computation process. The binary restrictions and the effect of diffraction are ignored in this process; therefore, the traditional methods<sup>33,34</sup> can be implemented to solve this problem.

Then, the following holographic problem is sequentially solved for each group of  $G$  adjacent binary projection patterns:

$$\begin{cases} \min \quad L = \sum_{\vec{x} \in A} |d_h - \mu(\vec{x})I(\vec{x})\Delta t|^2 \\ \quad + \sum_{\vec{x} \in \tilde{A}} |\mu(\vec{x})I(\vec{x})\Delta t - d_l|^2 \\ \text{s. t.} \quad I = \sum_{\phi \in \{\phi_g\}} I_\phi^{\text{temp}} + \sum_{\phi_g} |\mathcal{H}_{\phi_g}(\delta_{\phi_g} u)|^2, \\ \quad \delta_{\phi_g} \in \{0, 1\}, \quad g \in \{1, 2, \dots, G\} \end{cases}$$

Here the loss function is the same as that in the previous problem.  $I_\phi^{\text{temp}}$  is initialized as  $I_\phi^{\text{coarse}}$  and will be updated to be  $|\mathcal{H}_{\phi_g}(\delta_{\phi_g} u)|^2$  after  $\delta_{\phi_g}$  is holographically optimized.  $\{\phi_g\}$  is a set of adjacent  $G$  angles centred at  $\phi$ .  $\delta_{\phi_g}$  is the binary image shown by the DMD for the angle  $\phi_g$ .  $u$  represents the non-uniform amplitude distribution of the beam, which can be calibrated using a beam profiler.  $\mathcal{H}_{\phi_g}$  represents the process of light propagation in wave optics considering the refraction at the surface of air and material.

To solve this discrete optimization in the complex number domain, a virtual complex amplitude  $V_\phi$  is introduced to represent the average power of these  $G$  binary projections. It satisfies the condition that  $|V_\phi|^2 \approx \sum_{\phi_g} |\delta_{\phi_g} u|^2 / G$ . Within each iteration, the phase of  $\mathcal{H}_{\phi_g} V_\phi$  is assumed to be constant and the binarization error is temporarily ignored, that is  $|\mathcal{H}_{\phi_g} V_\phi|^2 \approx \sum_{\phi_g} |\mathcal{H}_{\phi_g}(\delta_{\phi_g} u)|^2 / G$ , thus the gradient descent of  $V_\phi$  can be approximated. Then  $V_\phi$  is updated along its gradient-descent direction and converted to its nearest positive real number.

The image set  $\{\delta_{\phi_g}\}$  is calculated by  $\delta_{\phi_g} = \{ |V_\phi|^2 \geq (g - 0.5) / G \cdot |u|^2 \}$  and the best  $\{\delta_{\phi_g}\}$  that minimizes the loss function is selected as the output. The flow chart of the holographic optimization is demonstrated in Extended Data Fig. 4a. Notably, directly converting a greyscale projection into a sequence of binary projections results in degraded intensity contrast for out-of-focus planes, because the light beams projected at different time points lack coherence to each other. Consequently, the intensity of direct projection  $|\mathcal{H}_\phi V_\phi|^2$  differs from that of the incoherent synthesis of binary projections  $\sum_{\phi_g} |\mathcal{H}_{\phi_g}(\delta_{\phi_g} u)|^2 / G$ , as shown in Extended Data Fig. 4b. The incoherent synthesis more accurately

represents our experimental implementation, thereby reducing dose estimation errors.

In the printing experiments, a volume pixel size of  $5.4 \mu\text{m}$  was used to match the DMD pixel size at the conjugate plane. In the simulations depicted in Fig. 2 and Extended Data Figs. 5 and 6, a volume pixel size of  $1.8 \mu\text{m}$  was used. A total of 180 greyscale images were derived from the traditional algorithms and the binarization parameter  $G$  was set to 10, yielding 1,800 binary projections to minimize the effect of motion blur. Each group underwent 20 holographic optimization cycles. For a model with dimensions  $1,350 \times 1,350 \times 1,852$  (corresponding to  $7.3 \times 7.3 \times 10.0 \text{ mm}$ ), our implemented holographic algorithm<sup>49</sup>, using the parameters mentioned above, required approximately 24 h to complete in MATLAB R2023a, running on an Intel Core i7-11700 CPU. Deep learning methods and GPUs may be used in the future to accelerate the computing process.

## Materials used for printing

**PEGDA hydrogel.** 20% w/v PEGDA with an average molecular weight of  $1,000 \text{ g mol}^{-1}$  (PEGDA 1000, P902470, Macklin) was dissolved in deionized water. 0.25% w/w of lithium phenyl-2,4,6-trimethylbenzoylphosphinate (LAP; L157759, Aladdin) was added as a photoinitiator. This solution was used for Fig. 1c, Extended Data Fig. 9d and Supplementary Video 1.

**PEGDA mixed solvent.** 20% w/v PEGDA 1000, 20% w/v deionized water and 60% polyethylene glycol with an average molecular weight of  $400 \text{ g mol}^{-1}$  (PEG 400, P815616, Macklin) were mixed and stirred for 30 min. 0.25% LAP was added as a photoinitiator. This gel was used for Figs. 4a-f and 5b,c, Extended Data Fig. 9a,b,e,k and Supplementary Video 2. PEGDA mixed solvent ink was used to characterize the performance of DISH. PEG can serve as porogen<sup>50</sup> and causes polymerization-induced phase separation in the printed samples. Although the polymer frameworks are still formed by PEGDA, the samples appear white instead of transparent owing to the scattering induced by phase separation. The enhanced scattering makes the printouts more visible and the printing process can thus be directly captured by cameras. Also, binary solvents could induce faster polymerization than a single solvent<sup>51</sup> and faster curing is suitable for DISH to increase the printing speed.

**PEGDA resin.** 2 mM photoinitiator diphenyl (2,4,6-trimethylbenzoyl) phosphine oxide (TPO; T107643, Aladdin) was added to PEGDA with an average molecular weight of  $1,000 \text{ g mol}^{-1}$  (P131592, Aladdin) and stirred until fully dissolved. This material was used to print objects in Figs. 1b, 4l-o and 5e-h, Extended Data Fig. 9f,g,i,j,l,m and Supplementary Videos 3 and 4.

**SilMA hydrogel.** SilMA was synthesized following the protocol in ref. 52. 2 g SilMA was dissolved in deionized water to make a 10-mL solution. The 20% w/v SilMA was used with 0.25% LAP and the printouts are shown in Extended Data Fig. 9o.

**GelMA hydrogel.** GelMA was synthesized following the protocol in ref. 53. 1 g GelMA was dissolved in deionized water to make a 10-mL solution. The 10% w/v SilMA was used with 0.25% LAP and the printouts are shown in Fig. 5k.

**BPAGDA resin.** BPAGDA (411167, Sigma) was mixed at 3:2 w/w with 2-hydroxyethyl methacrylate (HEMA; H810855, Macklin). 2 mM TPO was added and the mixture was stirred at  $60^\circ\text{C}$  for 30 min. The printouts are shown in Fig. 5j.

**DPHA resin.** DPHA (D889657, Macklin) was mixed at 2:1 w/w with HEMA. 2 mM TPO was added and the mixture was stirred at  $60^\circ\text{C}$  for 30 min. The printouts are shown in Fig. 5i and Extended Data Fig. 9n.

# Article

**UDMA resin.** UDMA (D885973, Macklin) was mixed at 4:1 w/w with HEMA. 2 mM TPO was added and the mixture was stirred at 40 °C for 30 min. The printouts are shown in Extended Data Fig. 9c,p.

**UDMA+PEGDA resin.** UDMA was mixed at 1:1 w/w with PEGDA. 2 mM TPO was added and the mixture was stirred at 40 °C for 30 min. The printouts are shown in Extended Data Fig. 9h.

The viscosity of the inks was tested by Anton Paar MCR 302e, rotor CP50, shearing rate 100 s<sup>-1</sup>. The viscosities of these materials are: 20% PEGDA hydrogel: 4.734 cP; 20% SilMA hydrogel: 40.12 cP; PEGDA mixed solvent: 63.85 cP; PEGDA resin: 99.11 cP; BPAGDA resin: 656.38 cP; DPHA resin: 750.49 cP; UDMA resin: 562.99 cP. These samples were tested at room temperature (25 °C). 10% GelMA hydrogel was used and tested at 40 °C as a liquid ink and the viscosity is 14.15 cP.

## Printing and post-processing

The inks can be directly replaced for each printing process and resin reuse could be achieved through heating and exposure to ambient air, as demonstrated in previous volumetric printing systems. Furthermore, low-viscosity materials used for printing, such as PEGDA aqueous solution, facilitate the spontaneous replenishment of dissolved oxygen. Gentle pipetting between printing sessions was conducted to maintain the printing performance for these low-viscosity inks.

The printouts were gently separated from the uncured materials and washed with water or ethanol. For high-viscosity resins, heating and ultrasonics could be involved to aid cleaning. Subsequently, an extra 405-nm light exposure (30 mW cm<sup>-2</sup>) was applied for 60 s in corresponding photoinitiator solutions (water containing 0.25% LAP or ethanol containing 2 mM TPO). For hydrogel samples, dipotassium hydrogen phosphate solution (9.7% w/v) was used to balance the swelling in Fig. 4 and Extended Data Fig. 9a,b, making the microscopic length the same as the designed length.

## Visualization of the printed products

In Supplementary Videos 1 and 2, the products were directly imaged within the material. In Supplementary Video 1, the subtle variation in refractive index was visualized by placing a checkerboard pattern behind the container. In Supplementary Video 2, a green laser beam was used to enhance scattering without influencing the curing reaction. In Supplementary videos 3 and 4, the cleaning process is temporarily put in a cuvette for better filming, with usual washing using bigger containers and more solvent to ensure cleanliness.

The products were post-processed and then photographed in various ways: macro photography (Figs. 1b, 4a,j,k,m and 5g–k and Extended Data Fig. 9b left, 9f,j–p), stereoscopy (Fig. 5e,f and Extended Data Fig. 9c,i) and bright-field microscopy (Figs. 1c right and 4a–f,h,i,n,o and Extended Data Fig. 9a,b,d,e,g). The hollow structure was validated by injecting different colours of ink, including Fig. 5h,k and Extended Data Fig. 9g,i,o. The X-ray computed tomography scanning in Extended Data Fig. 9h was conducted using a ZEISS Xradia 620 Versa.

All dimensions of the printed objects are reported as mean  $\pm$  standard deviation. For the linewidths in Fig. 4a,b,  $n = 20$  measurements were

taken for each stripe group across the sample. Data in Fig. 4g were obtained at each indicated axial position, with  $n = 6$  measurements per position. For the fishbone width in Fig. 4i,  $n = 10$  measurements were performed. For the conch structure in Fig. 4m–o, a total of  $n = 40$  measurements was conducted across its various lines.

## Reporting summary

Further information on research design is available in the Nature Portfolio Reporting Summary linked to this article.

## Data availability

All relevant data are publicly available on GitHub <https://github.com/sugar10w/DISH>. Source data are provided with this paper.

## Code availability

The codes for the pipeline and optimization algorithms of DISH with example data are publicly available on Zenodo (<https://doi.org/10.5281/zenodo.17905914>)<sup>49</sup> and GitHub (<https://github.com/sugar10w/DISH>).

49. Wang, X. Codes for digital incoherent synthesis of holographic light fields (DISH). Zenodo <https://doi.org/10.5281/zenodo.17905914> (2025).
50. Mandsberg, N. K., Aslan, F., Dong, Z. & Levkin, P. A. 3D printing of reactive macroporous polymers via thiol-ene chemistry and polymerization-induced phase separation. *Chem. Commun.* **60**, 5872–5875 (2024).
51. Beiler, B., Sáfrány, Á., Bató, L., Szomor, Z. & Veres, M. Effect of binary porogen mixtures on polymer monoliths prepared by gamma-radiation initiated polymerization. *Helijon* **10**, e38852 (2024).
52. Kim, S. H. et al. 3D bioprinted silk fibroin hydrogels for tissue engineering. *Nat. Protoc.* **16**, 5484–5532 (2021).
53. Yue, K. et al. Synthesis, properties, and biomedical applications of gelatin methacryloyl (GelMA) hydrogels. *Biomaterials* **73**, 254–271 (2015).

## Acknowledgements

We thank Y. Zhang for helpful discussions of printing materials. This work was supported by the Natural Science Foundation of China (62525506, 62088102, 62222508, 62125106), Beijing Natural Science Foundation (Z240011), New Cornerstone Science Foundation through the XPLORE PRIZE, and Beijing Key Laboratory of Cognitive Intelligence.

**Author contributions** J.W., Q.D. and X.W. conceived the research. X.W., Y.N., B.X., A.Z., Y.C. and J.W. designed and built the experimental set-up. Y.M., Y.N. and W.W. developed the printing materials and post-processing protocols. X.W., Y.N. and J.W. designed and refined the algorithms. X.W., Y.M., Y.N., B.X., A.Z. and Y.C. performed the 3D printing experiments. X.W., Y.M., Y.N., G.Z. and J.W. conducted sample characterization, data visualization and prepared the figures. X.W., Y.M. and Y.N. wrote the original manuscript. J.W. and Q.D. reviewed and edited the manuscript. J.W., L.F. and Q.D. acquired the funding and supervised the project. All authors have reviewed and approved the final manuscript.

**Competing interests** Q.D., X.W., B.X. and J.W. hold patents on technologies related to the DISH technology developed in this work. The other authors declare no competing interests.

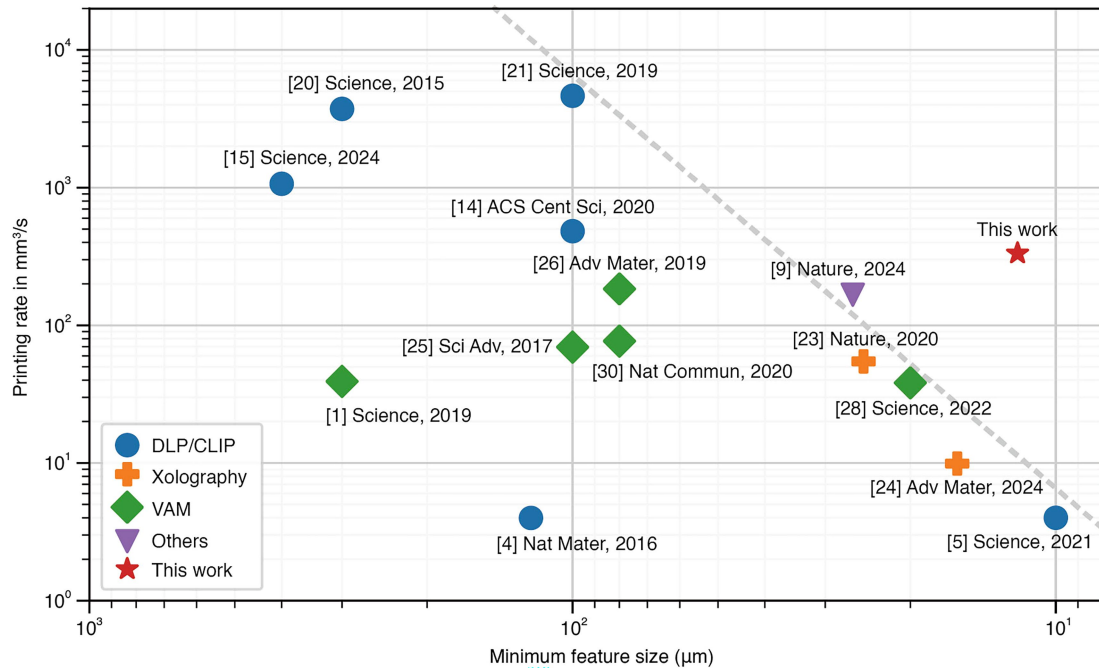
## Additional information

**Supplementary information** The online version contains supplementary material available at <https://doi.org/10.1038/s41586-026-10114-5>.

**Correspondence and requests for materials** should be addressed to Lu Fang, Jiamin Wu or Qionghai Dai.

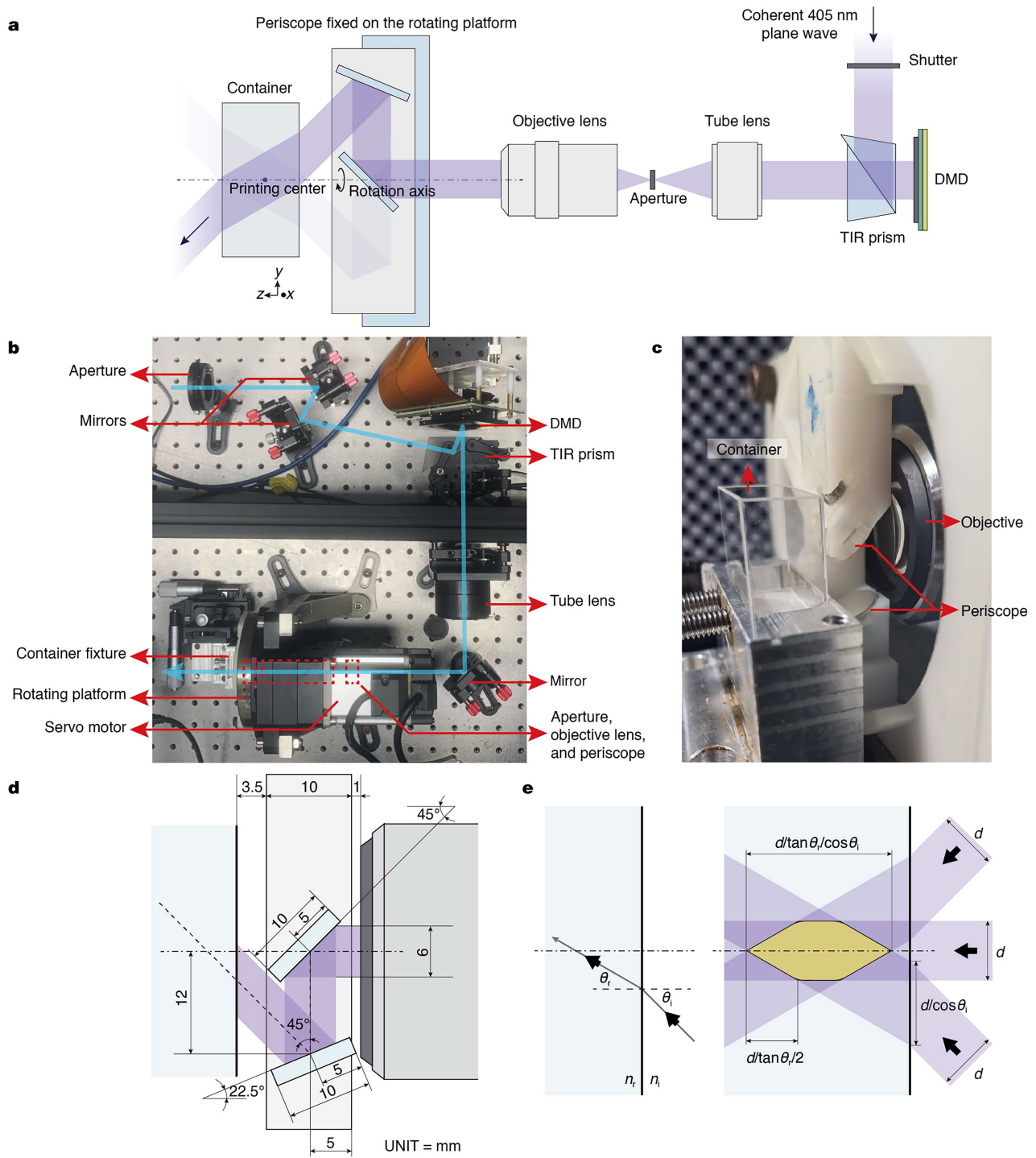
**Peer review information** *Nature* thanks Bastian Rapp, Maxim Shusteff and the other, anonymous, reviewer(s) for their contribution to the peer review of this work. Peer reviewer reports are available.

**Reprints and permissions information** is available at <http://www.nature.com/reprints>.



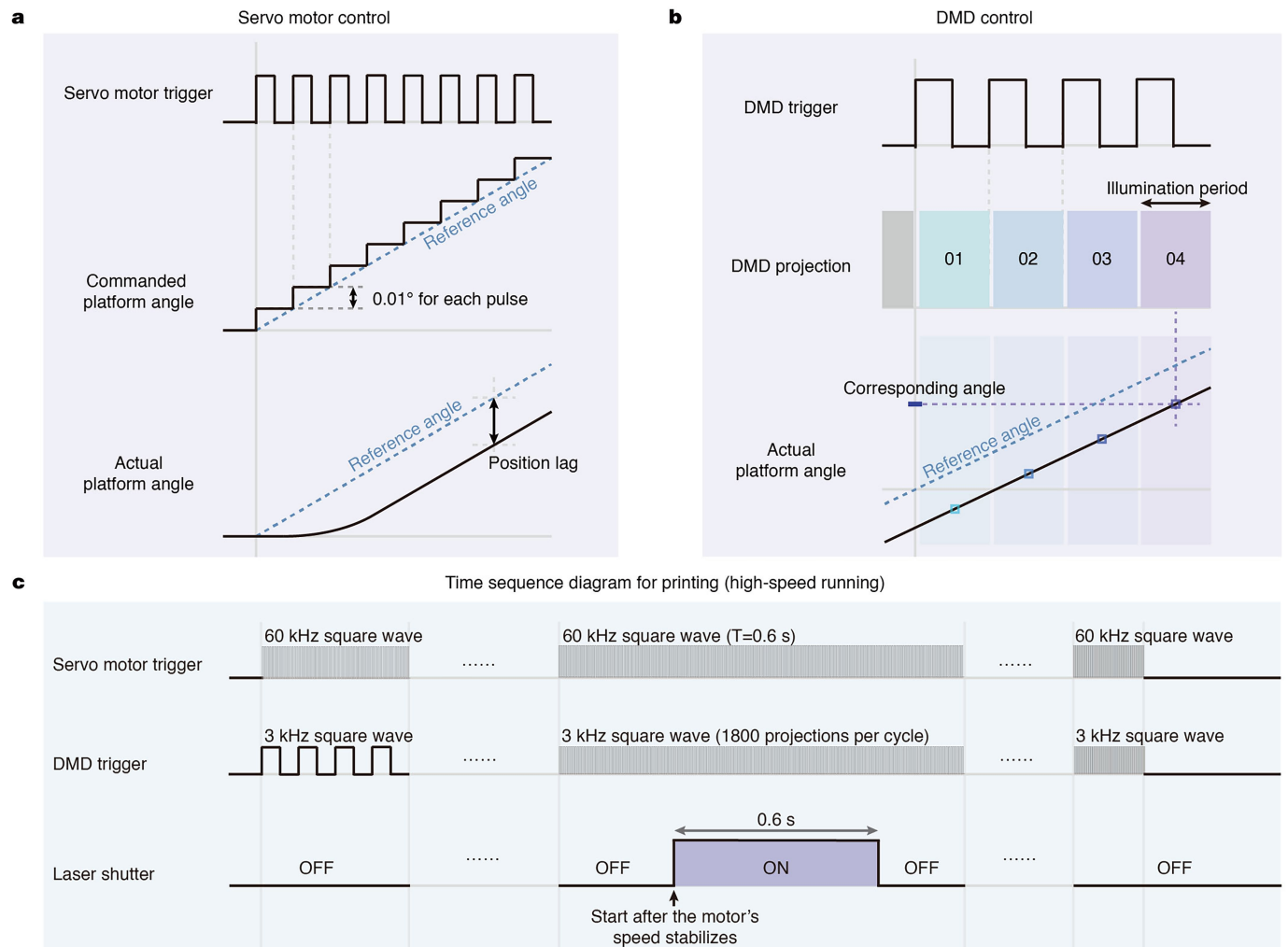
**Extended Data Fig. 1 | Benchmarking of DISH and state-of-the-art 3D printing methods.** We compare the volumetric printing rate and the corresponding minimum feature sizes for several 3D printing methods. The dashed line

represents a voxel printing rate of  $6.5 \times 10^6$  voxels  $s^{-1}$ , estimated under the assumption that the voxels in these works are cubes with the side length equal to the minimum feature size.



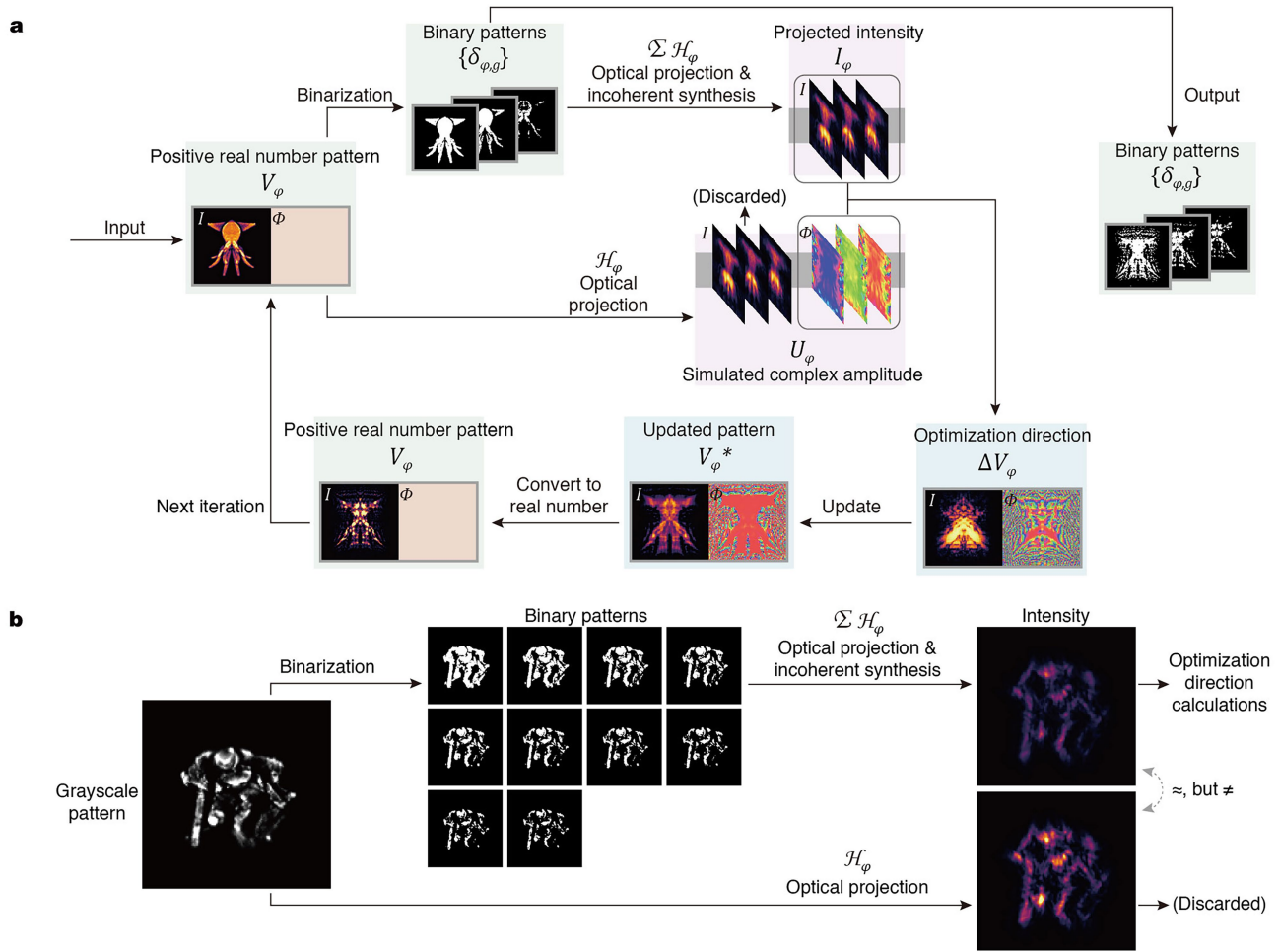
**Extended Data Fig. 2 | Schematic and experimental set-up of DISH.**  
**a**, Schematic of the optical path of DISH. **b**, Experimental system of DISH. The trajectory of the light beam is marked by blue lines. **c**, A close-up image illustrating the structure of the periscope integrated with a rotating platform.

**d**, Detailed mechanical design of the periscope. **e**, The printing area exhibits a centrally symmetric spindle-like shape.  $\theta_i$  represents the incident angle,  $\theta_r$  represents the refracted angle and  $d$  represents the beam diameter.

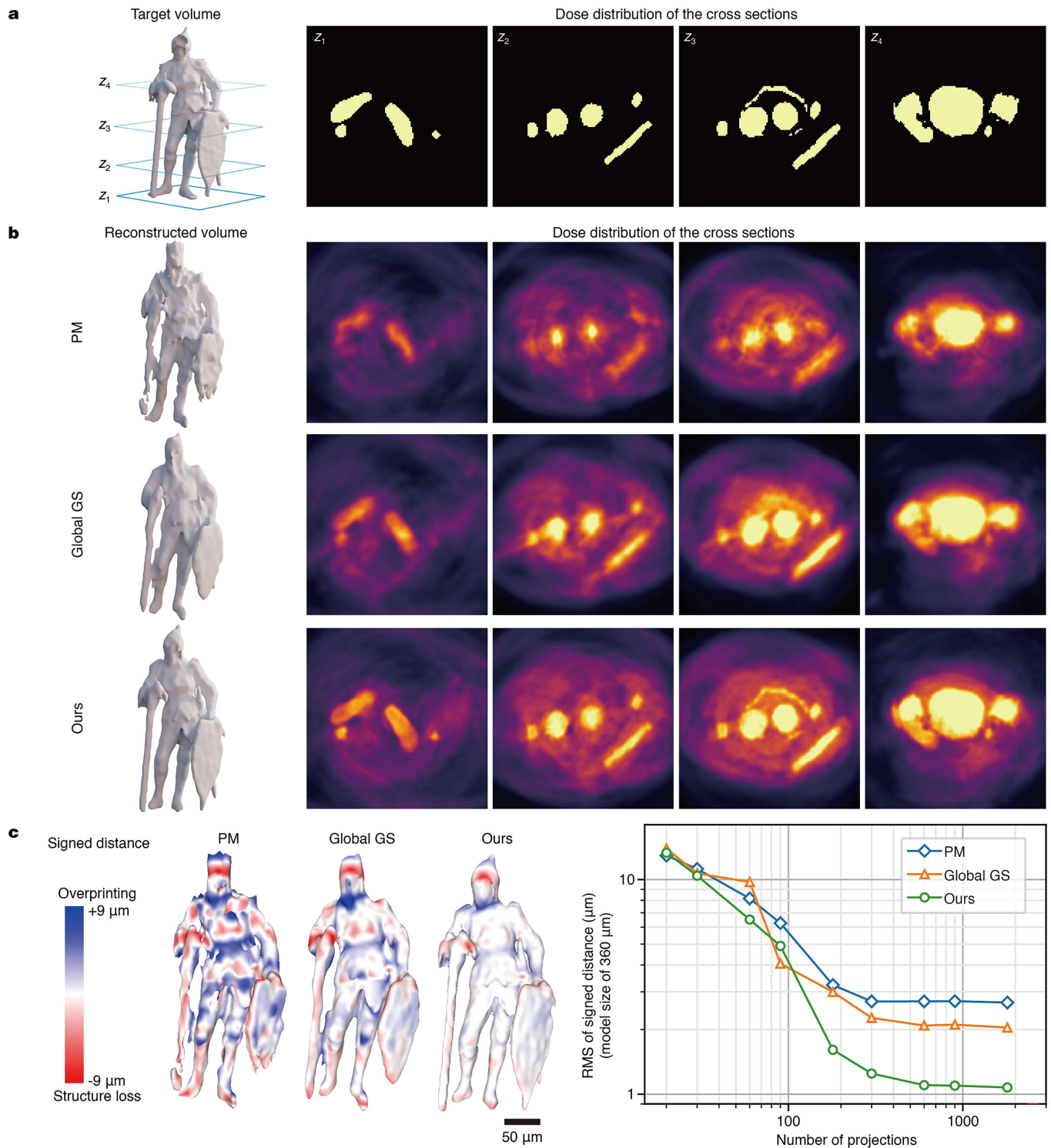


**Extended Data Fig. 3 | Time sequence diagrams for the synchronization of the laser, motor and DMD.** **a**, The servo motor trigger determines the position of the rotating platform. There is a position lag between the actual platform

angle and the commanded angle. **b**, Illustration of the DMD control. **c**, Overall time-sequence diagram used for printing.

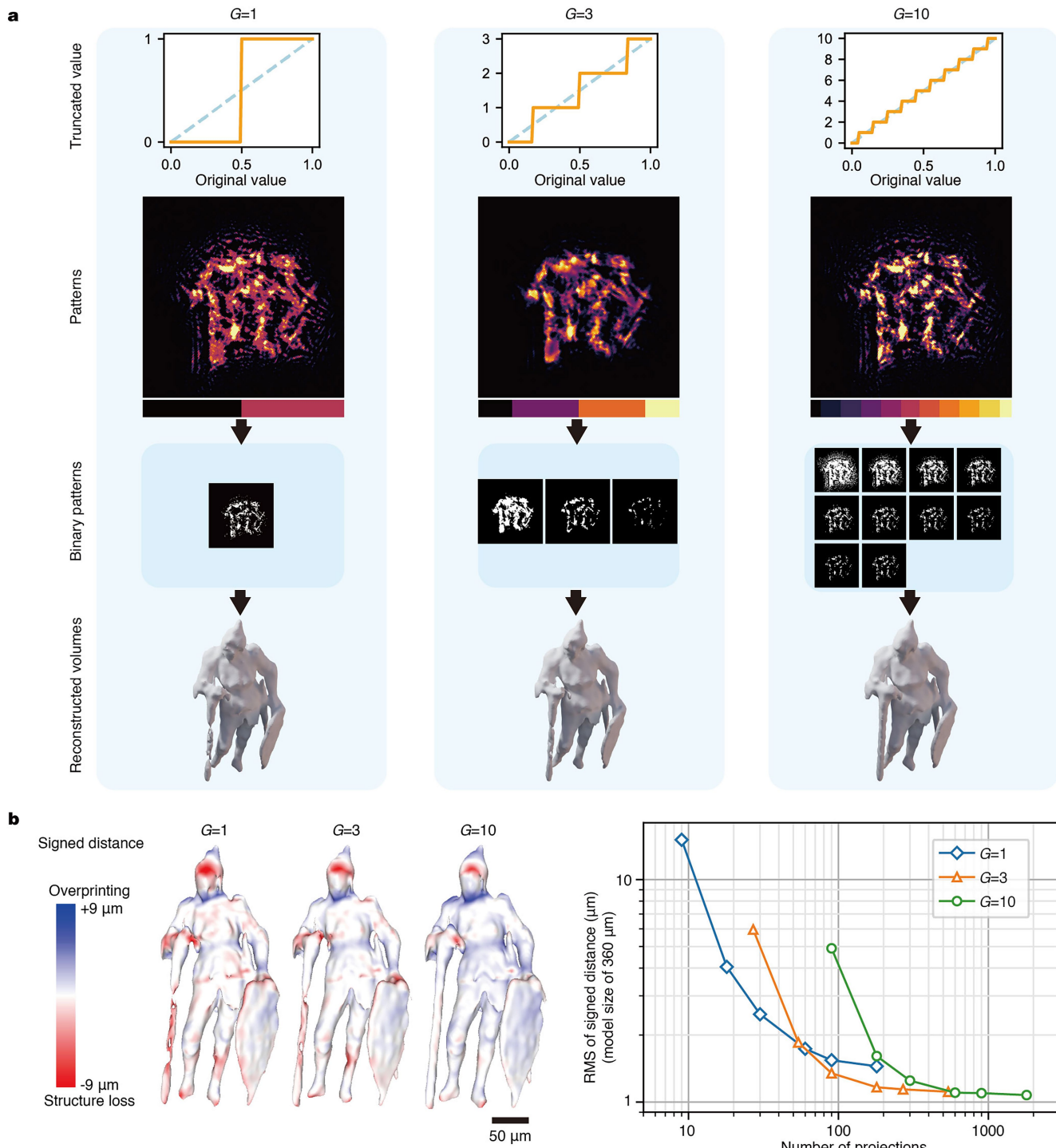


**Extended Data Fig. 4 | Flow chart of the holographic optimization for the binary patterns of each angle. a,** Flow chart of the gradient-descent-based holographic algorithm. **b,** Simulation for binarization-induced intensity error at the out-of-focus plane, illustrating the necessity of the holographic model during calculation.



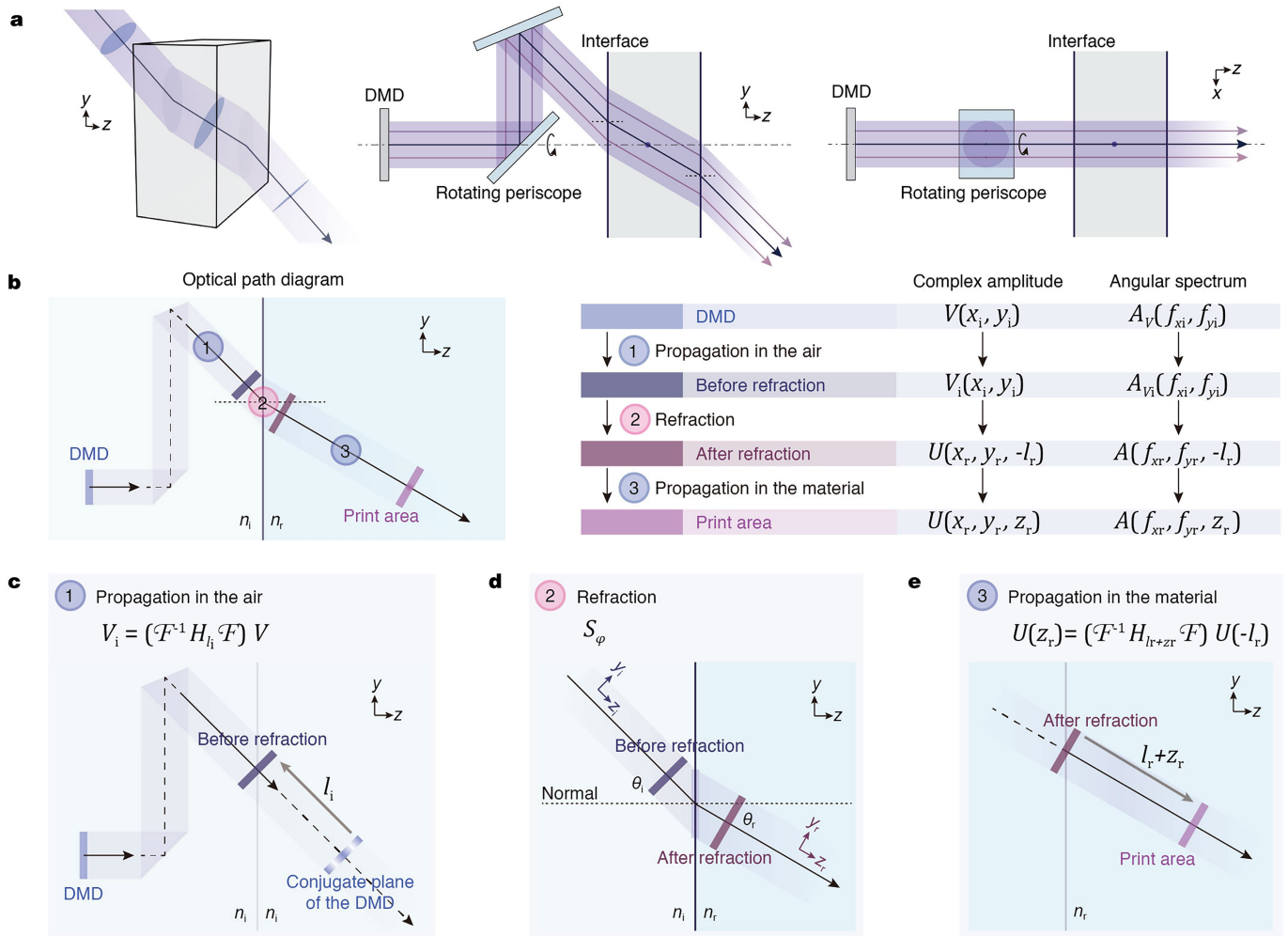
**Extended Data Fig. 5 | Comparative analysis of several pattern-optimization algorithms.** **a**, Illustration of the ground-truth target volume and its cross-sections. **b**, Simulated printing results obtained by several optimization methods illustrated with their cross-sections. The methods include PM used in previous CAL methods with ray optics modelling, the global Gerchberg–Saxton (GS)

algorithm and our binary holographic optimization algorithm. **c**, The signed distances of the simulated printing results compared with the ground truth (1,800 binary projections used). Curves of the root mean square of signed distances versus the number of total binary projection patterns used for different algorithms are shown on the right.



**Extended Data Fig. 6 | Illustration and evaluation of the binarization process for DMD patterns.** **a**, Illustration of different binarization parameters  $G$ , corresponding to the number of binary images used for a single greyscale image. The curves of the truncation function are shown at the top. The optimized greyscale pattern for a specific angle is shown on the second row, with the corresponding optimized binary patterns shown on the third row. The simulated

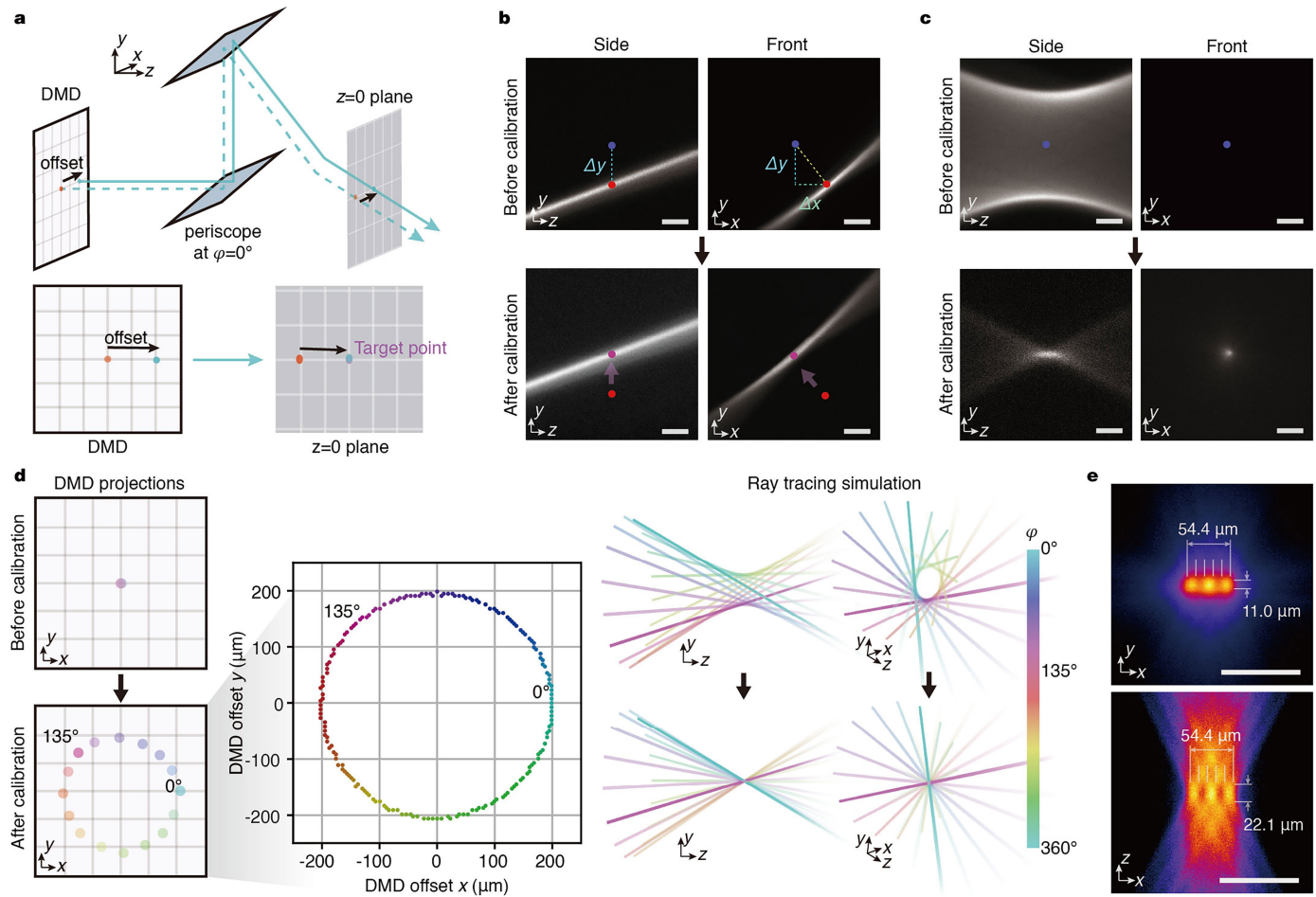
products by DISH are shown at the bottom. **b**, The signed distances of the simulated products, compared with the ground truth, corresponding to one, three and ten binary projections as a group. Curves of the root mean square of signed distances versus the number of total binary projection patterns with different binarization parameters are shown on the right.



**Extended Data Fig. 7 | Wave-optics model of the beam propagation in DISH.**

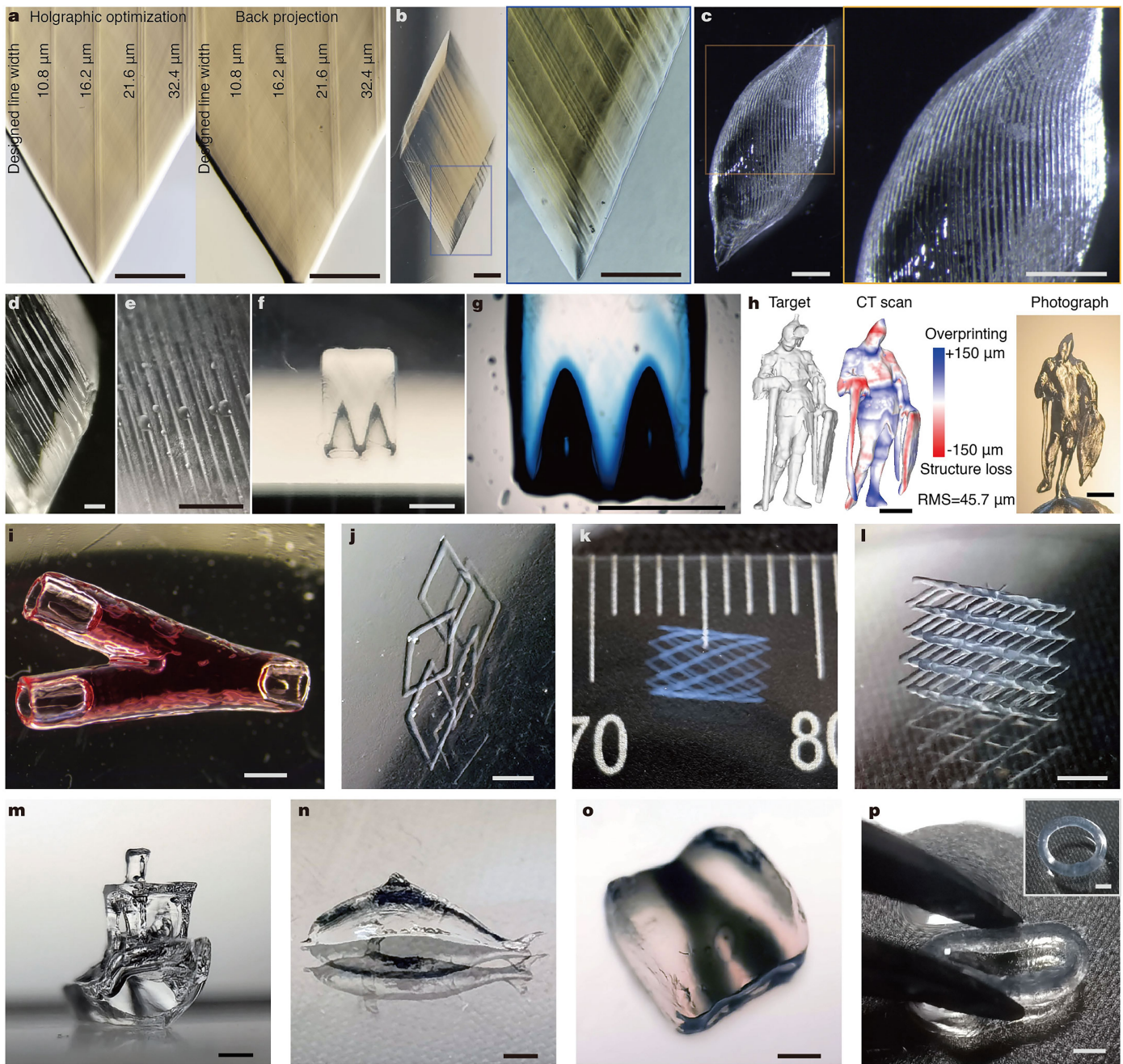
**a**, Illustration of the beam path of DISH for a specific angle. As illustrated from different viewpoints, the refracted beams are stretched along one axis owing to refraction and are less affected for another axis. **b**, The optical path diagram illustrates three stages of the beam propagation process during modelling in the holographic optimization algorithm, including propagation in air, refraction at the interface and propagation in the material. **c**, Illustration of stage 1:

propagation in air. **d**, Illustration of stage 2: refraction at the interface. **e**, Illustration of stage 3: propagation in the material.  $\theta_i$  represents the incident angle,  $\theta_r$  represents the refracted angle,  $n_i$  represents the refractive index of the air,  $n_r$  represents the refractive index of the material,  $l_i$  represents the distance from the interface to the printing centre and  $z_r$  represents the propagation distance from the printing centre to the target location.



**Extended Data Fig. 8 | Illustration of the adaptive-optics-based calibration process.** **a**, Schematic diagrams depicting the beam path during calibration. The illustrated calibration process aims to shift the intersection point of the beam at the  $z=0$  plane to the printing centre by introducing lateral offsets in optimized DMD patterns for each angle. **b**, The coordinates of the beam's intersection point at the  $z=0$  plane are determined by the images captured by

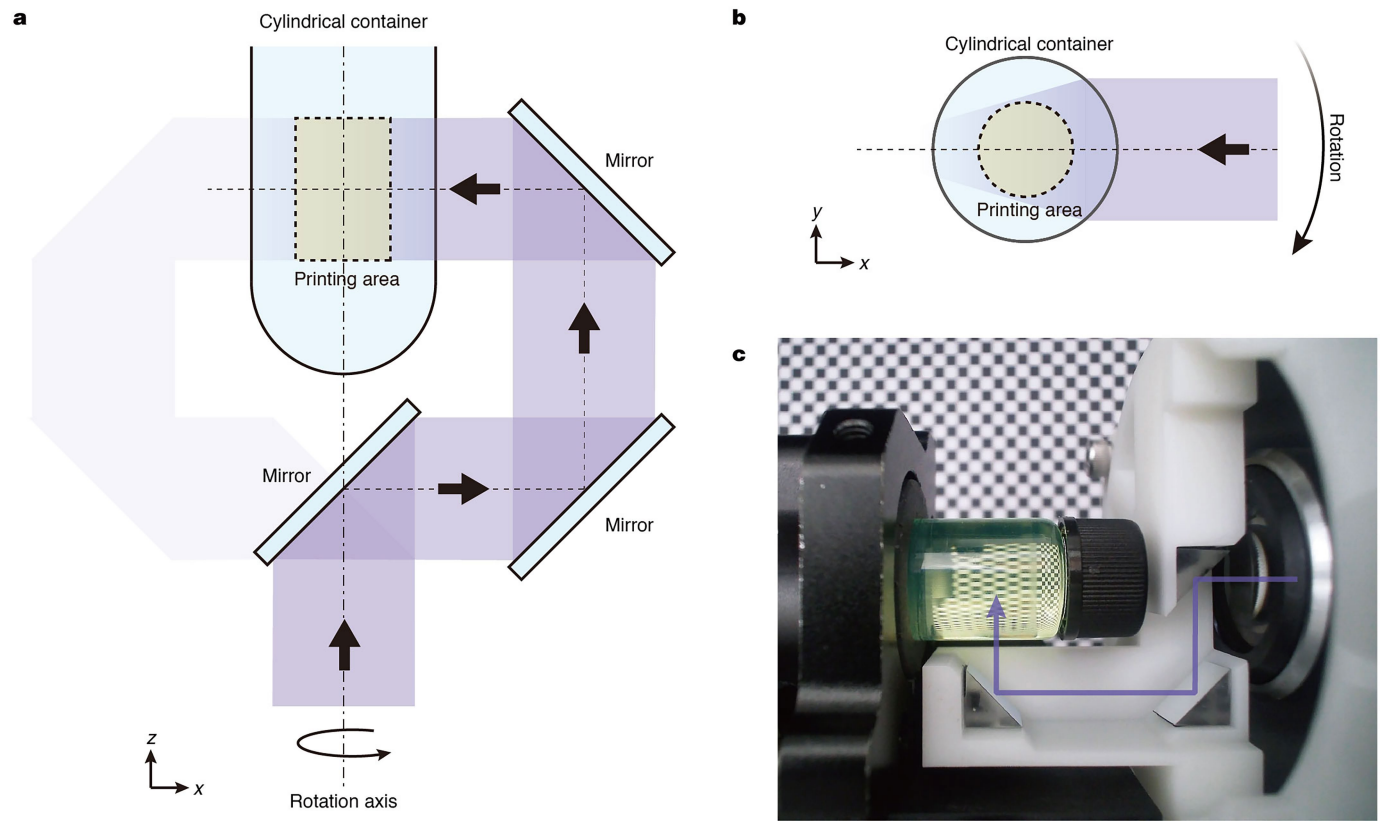
the side and front cameras. **c**, Time-lapse images demonstrate the beams for a single point before and after calibration. **d**, A series of DMD offsets are obtained for each projection angle, to ensure that the corresponding rays converge at the target point. The simulations of the ray tracing are shown on the right, illustrating the conditions before and after calibration. **e**, High-resolution patterns viewed from the front and side after calibration. Scale bars, 100  $\mu\text{m}$ .



**Extended Data Fig. 9 | High-resolution products of diverse structures and materials printed by DISH.** **a**, Experimental printed products with holographically optimized projections (left) and ray-approximation backprojections (right). **b**, Experimental printed products using the PEGDA-PEG–water mixture as the ink. The measured linewidths were  $32.0 \pm 2.1$ ,  $21.2 \pm 2.6$ ,  $16.4 \pm 1.6$  and  $75.0 \pm 3.0 \mu\text{m}$ . **c–e**, More stripe samples on curved and flat surfaces obtained by DISH. **f,g**, Inner conical model. The diameters of the

inscribed circles of the two cones at the vertex are about  $55.8 \mu\text{m}$  and  $49.7 \mu\text{m}$ , respectively. **h**, X-ray computed tomography scan of the sample of Theodoric. **i**, Bifurcated tubes. **j**, Diamond-shaped chains. **k,l**, 3D grid structures. **m**, Benchy model viewed from the side. **n**, Dolphin model printed with DPBA. **o**, Bifurcated tubes printed with soft biomaterial SiIMA. **p**, Ring printed with UDMA and its elastic deformation. The structure without deformation is shown in the inset. Scale bars, 1 mm (a–c,f–p); 100  $\mu\text{m}$  (d,e).

# Article



**Extended Data Fig. 10 | Mechanical design and implementation of orthogonal projections.** **a**, Diagram of the periscope for orthogonal projections to address the missing cone problem in the axial domain. **b**, Diagram illustrating the

refraction effects and the printing area in the cylindrical container. **c**, Photo of the proof-of-concept system.

## Reporting Summary

Nature Portfolio wishes to improve the reproducibility of the work that we publish. This form provides structure for consistency and transparency in reporting. For further information on Nature Portfolio policies, see our [Editorial Policies](#) and the [Editorial Policy Checklist](#).

### Statistics

For all statistical analyses, confirm that the following items are present in the figure legend, table legend, main text, or Methods section.

n/a Confirmed

- The exact sample size ( $n$ ) for each experimental group/condition, given as a discrete number and unit of measurement
- A statement on whether measurements were taken from distinct samples or whether the same sample was measured repeatedly
- The statistical test(s) used AND whether they are one- or two-sided
  - Only common tests should be described solely by name; describe more complex techniques in the Methods section.*
- A description of all covariates tested
- A description of any assumptions or corrections, such as tests of normality and adjustment for multiple comparisons
- A full description of the statistical parameters including central tendency (e.g. means) or other basic estimates (e.g. regression coefficient) AND variation (e.g. standard deviation) or associated estimates of uncertainty (e.g. confidence intervals)
- For null hypothesis testing, the test statistic (e.g.  $F$ ,  $t$ ,  $r$ ) with confidence intervals, effect sizes, degrees of freedom and  $P$  value noted
  - Give  $P$  values as exact values whenever suitable.*
- For Bayesian analysis, information on the choice of priors and Markov chain Monte Carlo settings
- For hierarchical and complex designs, identification of the appropriate level for tests and full reporting of outcomes
- Estimates of effect sizes (e.g. Cohen's  $d$ , Pearson's  $r$ ), indicating how they were calculated

*Our web collection on [statistics for biologists](#) contains articles on many of the points above.*

### Software and code

Policy information about [availability of computer code](#)

Data collection All data are collected and processed with MATLAB R2023a (Mathworks).

Data analysis All data processing and analysis were performed using MATLAB R2023a (Mathworks).

For manuscripts utilizing custom algorithms or software that are central to the research but not yet described in published literature, software must be made available to editors and reviewers. We strongly encourage code deposition in a community repository (e.g. GitHub). See the Nature Portfolio [guidelines for submitting code & software](#) for further information.

### Data

Policy information about [availability of data](#)

All manuscripts must include a [data availability statement](#). This statement should provide the following information, where applicable:

- Accession codes, unique identifiers, or web links for publicly available datasets
- A description of any restrictions on data availability
- For clinical datasets or third party data, please ensure that the statement adheres to our [policy](#)

All relevant data are publicly available on GitHub <https://github.com/sugar10w/DISH>

## Research involving human participants, their data, or biological material

Policy information about studies with [human participants or human data](#). See also policy information about [sex, gender \(identity/presentation\), and sexual orientation](#) and [race, ethnicity and racism](#).

### Reporting on sex and gender

Use the terms sex (biological attribute) and gender (shaped by social and cultural circumstances) carefully in order to avoid confusing both terms. Indicate if findings apply to only one sex or gender; describe whether sex and gender were considered in study design; whether sex and/or gender was determined based on self-reporting or assigned and methods used. Provide in the source data disaggregated sex and gender data, where this information has been collected, and if consent has been obtained for sharing of individual-level data; provide overall numbers in this Reporting Summary. Please state if this information has not been collected. Report sex- and gender-based analyses where performed, justify reasons for lack of sex- and gender-based analysis.

### Reporting on race, ethnicity, or other socially relevant groupings

Please specify the socially constructed or socially relevant categorization variable(s) used in your manuscript and explain why they were used. Please note that such variables should not be used as proxies for other socially constructed/relevant variables (for example, race or ethnicity should not be used as a proxy for socioeconomic status). Provide clear definitions of the relevant terms used, how they were provided (by the participants/respondents, the researchers, or third parties), and the method(s) used to classify people into the different categories (e.g. self-report, census or administrative data, social media data, etc.). Please provide details about how you controlled for confounding variables in your analyses.

### Population characteristics

Describe the covariate-relevant population characteristics of the human research participants (e.g. age, genotypic information, past and current diagnosis and treatment categories). If you filled out the behavioural & social sciences study design questions and have nothing to add here, write "See above."

### Recruitment

Describe how participants were recruited. Outline any potential self-selection bias or other biases that may be present and how these are likely to impact results.

### Ethics oversight

Identify the organization(s) that approved the study protocol.

Note that full information on the approval of the study protocol must also be provided in the manuscript.

## Field-specific reporting

Please select the one below that is the best fit for your research. If you are not sure, read the appropriate sections before making your selection.

Life sciences       Behavioural & social sciences       Ecological, evolutionary & environmental sciences

For a reference copy of the document with all sections, see [nature.com/documents/nr-reporting-summary-flat.pdf](https://nature.com/documents/nr-reporting-summary-flat.pdf)

## Life sciences study design

All studies must disclose on these points even when the disclosure is negative.

### Sample size

Describe how sample size was determined, detailing any statistical methods used to predetermine sample size OR if no sample-size calculation was performed, describe how sample sizes were chosen and provide a rationale for why these sample sizes are sufficient.

### Data exclusions

Describe any data exclusions. If no data were excluded from the analyses, state so OR if data were excluded, describe the exclusions and the rationale behind them, indicating whether exclusion criteria were pre-established.

### Replication

Describe the measures taken to verify the reproducibility of the experimental findings. If all attempts at replication were successful, confirm this OR if there are any findings that were not replicated or cannot be reproduced, note this and describe why.

### Randomization

Randomization was not relevant to this study, because no experimental groups were formed.

### Blinding

Blinding was not relevant to this study, because no group allocation was performed.

## Reporting for specific materials, systems and methods

We require information from authors about some types of materials, experimental systems and methods used in many studies. Here, indicate whether each material, system or method listed is relevant to your study. If you are not sure if a list item applies to your research, read the appropriate section before selecting a response.

## Materials &amp; experimental systems

n/a	Involved in the study
<input checked="" type="checkbox"/>	Antibodies
<input checked="" type="checkbox"/>	Eukaryotic cell lines
<input checked="" type="checkbox"/>	Palaeontology and archaeology
<input checked="" type="checkbox"/>	Animals and other organisms
<input checked="" type="checkbox"/>	Clinical data
<input checked="" type="checkbox"/>	Dual use research of concern
<input checked="" type="checkbox"/>	Plants

## Methods

n/a	Involved in the study
<input checked="" type="checkbox"/>	ChIP-seq
<input checked="" type="checkbox"/>	Flow cytometry
<input checked="" type="checkbox"/>	MRI-based neuroimaging

## Plants

## Seed stocks

Report on the source of all seed stocks or other plant material used. If applicable, state the seed stock centre and catalogue number. If plant specimens were collected from the field, describe the collection location, date and sampling procedures.

## Novel plant genotypes

Describe the methods by which all novel plant genotypes were produced. This includes those generated by transgenic approaches, gene editing, chemical/radiation-based mutagenesis and hybridization. For transgenic lines, describe the transformation method, the number of independent lines analyzed and the generation upon which experiments were performed. For gene-edited lines, describe the editor used, the endogenous sequence targeted for editing, the targeting guide RNA sequence (if applicable) and how the editor was applied.

## Authentication

Describe any authentication procedures for each seed stock used or novel genotype generated. Describe any experiments used to assess the effect of a mutation and, where applicable, how potential secondary effects (e.g. second site T-DNA insertions, mosaicism, off-target gene editing) were examined.